Modeling intercalation in cathode materials with phase-field methods: Assumptions and implications using the example of LiFePO$_4$

Simon Daubner[a,*], Marcel Weichel[a], Daniel Schneider[a,b], Britta Nestler[a,b]

[a]*Institute of Applied Materials (IAM-MMS, previously IAM-CMS), Karlsruhe Institute of Technology (KIT), Strasse am Forum 7, 76131 Karlsruhe, Germany*
[b]*Institute of Digital Materials Science (IDM), Karlsruhe University of Applied Sciences, Moltkestr. 30, 76133 Karlsruhe, Germany*

Abstract

The multiphase-field method has great potential to advance future research on battery materials. In this work, we discuss the modeling of phase-separating intercalation compounds based on the Cahn-Hilliard equation as well as a multi-phase, multi-component model operating in an Allen-Cahn framework. Modeling assumptions are introduced step-by-step to facilitate future developments and bridging the gap across scales. Dimensionality reduction reflecting the material anisotropies can be critical for combining the phase-field approach with Newman-type models. Furthermore, we discuss a nano-particle battery model starting from intercalation in a defect-free, single-crystalline platelet. The underlying modelling assumptions are reduced step-by-step, first, including in-plane diffusion as a result of crystal defects and finally accounting for a polycrystalline material section. We show how faster in-plane diffusion promotes phase separation while higher C-rates and coherency strain lead to the opposite effect. This work highlights the importance to consider pre-existing grain boundaries for nucleation at higher-order junctions, heterogeneity of the intercalation fluxes and grain-by-grain filling behaviour. Anisotropic elastic deformation leads to high stresses at the evolving phase boundaries, especially at high misorientations between neighbouring grains. The maximum principle stress is used as an estimate for degradation by fracture in polycrystals.

Keywords: multiphase-field method, phase separation, intercalation, LFP

1. Introduction

Phase transformations and ordering effects in cathode materials can lead to a multitude of energetically favourable states marked by coexistence of phases and, thus, plateaus in the open-circuit voltage. A very well-known example is the commercialized, phase separating LiFePO$_4$ (LFP) [1], but also very promising cathode materials for sodium-ion intercalation batteries feature phase separation and pronounced volumetric

---

*simon.daubner@kit.edu
Email address: `simon.daubner@kit.edu` (Simon Daubner)

expansion upon cycling due to the larger ionic radius of sodium [2, 3]. Typically, these materials are based on a reversible intercalation mechanism and have highly anisotropic properties on the crystalline scale. Degradation mechanisms such as fracture and disintegration of agglomerated particles strongly depend on the primary particle size and morphology which is why, in this context, the discussion of particle morphology is crucial for battery performance. Taylored design of agglomerated particles and the overall electrode structure can lead to beneficial multi-particle behaviour and influence overpotential, percentage of active particle population, accessible capacity, rate capability and other kinetic aspects [4]. The strongly coupled effects of electro-chemical and mechanical driving forces on the microscale are difficult to access from experiments but simulations can help to shed some light on the local effects influencing the overall cell behaviour. While this endeavor can surely only be adressed by a combination of simulation approaches across the scales, we want to elaborate on the contribution of the phase-field method and point out links to other methods.

The multiphase-field method is a suitable tool to investigate the coupled effects of electro-chemo-mechanical driving forces on the transport processes of intercalated ions [5, 6]. Although, the phase-field approach originally emerged to study the microstructure evolution during solidification, it has been applied to a broad variety of fields up to date [7–9]. The accessible length scales that have been investigated in previous works range from few nanometers [10, 11] to several micrometers [12] and, by using high-performance computing, even up to the millimeter scale [13]. So technically, the multiphase-field approach should be able to cover battery simulations ranging from single crystals ($\sim 100\,\mathrm{nm}$) to agglomerates ($\sim 10\,\mu\mathrm{m}$) up to an electrode layer ($\sim 50\,\mu\mathrm{m}$) if the interfacial energy and interfacial width can be effectively decoupled [14].

Han $et\ al.$ [15] modelled diffusion of intercalated ions employing the phase-field method, motivated by the idea that Fickian diffusion is not sufficient to describe transport inside cathode particles with large concentration gradients as in the phase-separating $\mathrm{Li}_X\mathrm{FePO}_4$. This material exhibits a large miscibility gap which results in a voltage plateau over almost the entire composition range of $X \in [0, 1]$ at room temperature [1]. The regular solution free energy introduced in [15] is relatively simple, yet adequate to describe the neighbouring interactions of intercalated ions in the bulk. Following the principle of linear irreversible thermodynamics, the species flux is then driven by the gradient of diffusion potential, hence it could be shown that diffusion coefficients can be reliably determined by GITT measurements [15]. Since then, LFP has become the drosophila of many modeling efforts involving first-principle calculations [16–20], Kinetic Monte Carlo (KMC) simulations [21–23] and the phase-field method [5, 10, 11, 24–26].

Density Functional Theory (DFT) is tailored to investigate bulk properties of crystalline materials such as diffusivity, elastic constants, stable phases and the related equilibrium voltage curve. It can furthermore be employed to investigate the chemical interfacial energies between coherent phases as well as surface energies in vacuum. Morgan $et\ al.$ [16] used first-principle calculations to determine the diffusion path and associated energy barrier in LFP, predicting 1D diffusion and kinetic limitation due to electronic conductivity rather than Li diffusivity. This study was later extended to include defects in the crystal, in order to estimate

2

the particle size dependence [17]. The calculation of elastic constants [18] in combination with anisotropic chemical interfacial energies [19] can be used to estimate the thermodynamically stable interface orientation of the phase-separated state. The results are size- and morphology-dependent and based on the assumption of equilibrium, meaning that kinetic effects are neglected. These techniques are very helpful in identifying promising intercalation materials and predicting some of their inherent material properties.

While the above-mentioned material properties of intercalation compounds can be studied using first-principle calculations, there are many relevant phenomena with time and length scales that are only accessible using continuum methods like the phase-field approach [20]. Nucleation and growth, the interplay of chemical and mechanical driving forces as well as the collective behaviour of many interconnected particles are highly relevant but cannot be investigated by DFT. Efforts to bridge the gap between ab-initio simulations and phase-field studies based on empirical parameter fits have been undertaken using KMC [22]. This approach allows to study bulk and surface effects in small crystalline sections and is able to predict ordering, nucleation and growth behaviour purely based on DFT data. In this work, we want to elaborate if the direct scale bridging between phase-field and ab-initio methods is possible and check if the calculations are consistent with other investigations.

Therefore, we discuss two phase-field approaches and underlying assumptions that can be employed to gain a better understanding of the non-equilibrium behaviour of intercalation compounds. The first is based on the *Cahn-Hilliard equation* [27, 28] and well-suited to model bulk diffusion in single crystals including phase transformations on the same parent lattice (i.e. coherent interfaces between the phases). The second approach is the more general multiphase-field framework [8, 9, 14] based on *Allen-Cahn equations* for the evolution of non-conserved order parameters in combination with the evolution of diffusional potential based on the grand-chemical potential [29, 30]. This framework has been sucessfully combined with elastic driving forces based on jump conditions [31, 32] to model martensitic transformations [12], crack propagation [33–35] and the evolution of electric field to study electromigration [36]. It has further been shown that grain boundary diffusion [37] as well as the instability leading to phase separation in the miscibility gap [6] can be effectively modelled. The aim of this work is to show the potentials of both approaches for the numerical screening of promising intercalation electrode materials while also discussing their complementary range of applicability and their limitations due to modeling assumptions.

The remainder of this paper is organized as follows. In Sections 2.1 to 2.4, we discuss the underlaying electro-chemical modeling assumptions which are necessary to formulate the thermodynamic models in Sec. 2.5 and 2.6. There, we introduce two phase-field formulations that will be applied in the following simulation studies. Up to this point, the presented framework is very general in the sense that it can be applied for any kind of intercalation modeling and beyond. To discuss some model implications in more detail, we choose LFP, which has been well studied, as an example. Sec. 2.8 gives an overview of the available material data on LFP, mainly based on DFT calculations and additionally including experimental works.

3

In Sec. 3, we discuss the modeling of intercalation compounds. New findings are discussed in the context of their underlying assumptions as well as previously published results. The structure aims to guide the reader in a step-by-step manner, starting with implications of dimensionality reduction (3.1) and relaxation towards thermodynamic equilibrium via phase separation (3.2). The other two subsections complete this ensemble by the discussion of voltage hysteresis under galvanostatic charge and discharge in a single crystal (3.3) and, finally, in a polycrystalline slab (3.4).

2. Theory and simulation methods

In this section we introduce the thermodynamic basis to describe the evolution of composition in intercalation-type battery materials governed by electro-chemo-mechanical potentials. All the concepts will be directly applied for the case of intercalation compounds but can be generalized to other cases. The models are valid under the assumptions introduced in the following sections.

2.1. Lattice diffusion

The diffusion of polarons inside the intercalation compound is modeled based on linear irreversible thermodynamics and similar to interstitial diffusion inside a lattice. The maximal concentration of intercalated ions c_{max} is given by the number of interstitial sites per unit cell volume ($V_{UC} = abc$ for orthorombic cells). The sum of polarons and vacancies $\tilde{c}_i + \tilde{c}_j = c_{max}$ can be considered constant using the common assumption of negligible volumetric expansion upon intercalation. We then normalize the field variable by its maximal value and compute mole fractions $c_i = \tilde{c}_i/c_{max}$ (also called composition in the following). The general form of the reaction-diffusion equation which accounts for mass conservation including a production term R can be expressed as

$$\frac{\partial c}{\partial t} + \boldsymbol{\nabla} \cdot \boldsymbol{J} = R(c,t). \tag{1}$$

Throughout this work $\boldsymbol{\nabla} \cdot (\cdot)$ denotes the divergence and $\boldsymbol{\nabla}(\cdot)$ the gradient operator. In case of linear irreversible thermodynamics the mass flux is given by

$$\boldsymbol{J} = -\boldsymbol{M}(c)\boldsymbol{\nabla}\bar{\mu} \tag{2}$$

where $\bar{\mu}$ is the diffusion potential and includes electrical, chemical as well as mechanical effects. The gradient $\boldsymbol{\nabla}\bar{\mu}$ is the thermodynamic driving force for diffusion in the system. $\boldsymbol{M}(c)$ denotes the corresponding mobility function which is a second order tensor in the general anisotropic case and reduces to a scalar for purely isotropic diffusion. Furthermore, the function $\boldsymbol{M}(c)$ depends on the free energy formulation and is specified in Sec. 2.5 and 2.6.

4

2.2. Bulk electro-chemical potentials

We start from a generic expression of the electro-chemical potential $\tilde{\mu}$ of lithium ions

$$\tilde{\mu} = \mu^{\ominus} + RT\ln(a) + eN_A\Phi \tag{3}$$

where $\mu^{\ominus}$ denotes the reference chemical potential, a the activity and Φ the local electric potential, respectively. We apply Eq. (3) to the electrodes under certain assumptions, namely

- We consider metallic lithium as the anode (subscript A) in our system. There are no concentration variations and therefore, no entropic or enthalpic energy contributions. Fast motion of electrons leads to the same local electric potential everywhere in the anode.

- The cathode (subscript C) material LFP takes up lithium by an intercalation reaction and the free energy varies correspondingly with concentration. The entropic term is assumed to be an ideal solution as we model the filling of vacancies in a crystal lattice. The lithium ions exhibit some neighboring effects which are modelled via an enthalpic contribution. The electric potential is assumed to be constant across the cathode active material.

These assumptions lead to

$$\tilde{\mu}_A = \mu_A^{\ominus} + eN_A\Phi_A \tag{4}$$

$$\tilde{\mu}_C = \mu_C^{\ominus} + eN_A\Phi_C + RT(\ln(c) - \ln(1-c)) + h(c). \tag{5}$$

In thermodynamic equilibrium, the electro-chemical potentials are constant across the whole cell ($\tilde{\mu}_A = \tilde{\mu}_C$). The measurable open circuit potential $V_{OCV}(X)$ is related to the chemical potential difference in Fermi levels

$$\begin{aligned}
V_{OCV} &= (\Phi_C - \Phi_A)_{\text{eq.}} \\
&= \frac{\mu_A^{\ominus} - \mu_C^{\ominus}}{eN_A} - \frac{1}{V_C}\int \frac{k_B T}{e}\left(\ln\left(\frac{c}{1-c}\right)\right) + \frac{h(c)}{eN_A}\,dV_C
\end{aligned} \tag{6}$$

where we use the integral notation to account for phase-separated states in equilibrium and, therefore, integrate over the active cathode material volume V_C. $X \in [0,1]$ denotes the average filling fraction in Li$_X$FePO$_4$. Good fit for LFP is achieved if the first term $V_{\text{cell}}^{\ominus} = (\mu_A^{\ominus} - \mu_C^{\ominus})/(eN_A)$ takes the value of the voltage plateau and the enthalpic contribution is modelled as $h(x) = \Omega(1-2x)$ [24]. This choice corresponds to a regular solution free energy with enthalpy of mixing Ω and the corresponding open circuit voltage shown in Fig. 1a. Within the multi-phase approach, the regular solution is replaced by an interpolation of phase-dependent chemical free energy contributions [6]. These functions can be fitted such that the resulting open circuit potential matches experimental measurements close to the thermodynamic equilibrium as shown in Fig. 1b.
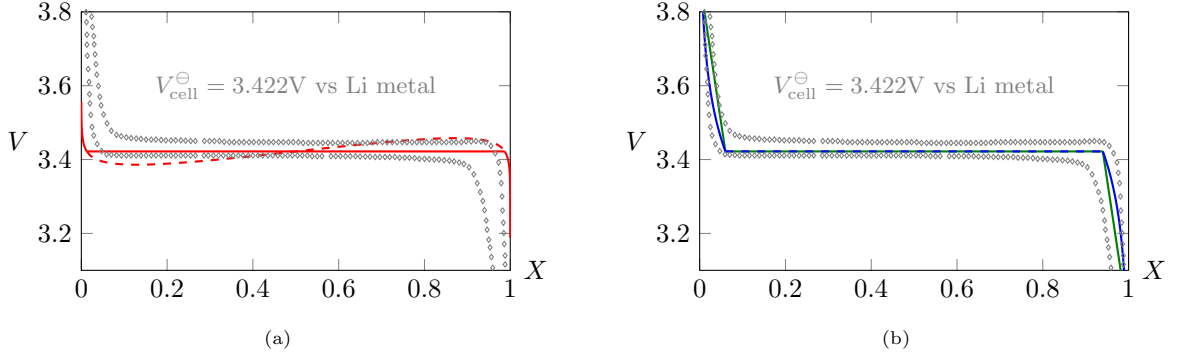
Figure 1: Open circuit potential V_{OCV} over filling fraction X in Li_XFePO_4. The gray data points are taken from Dreyer *et al.* [38] at C-rate 1/20 and mapped to the average filling fracion X under the assumption that all Li can reversibly inserted and extracted. A regular solution fit according to Eq. (6) with Ω taken from [10] is shown in a). Quadratic (green) and logarithmic (blue) chemical energy fits for the Allen-Cahn model formulation are shown in b).

2.3. Electro-chemical reaction

The driving force of the intercalation reaction $\text{Li}^+ + e^- + \text{FePO}_4 \rightarrow \text{LiFePO}_4$ is given by the difference in electro-chemical potentials at the interface between electrolyte (E) and the cathode $\tilde{\mu}_E - \tilde{\mu}_C$. Under the assumption of fast reaction at the anode as well as fast transport in the electrolyte ($c_E = $ const. and $\Phi_E = $ const. around the particle), we can approximate the driving force by

$$\frac{\tilde{\mu}_A - \tilde{\mu}_C}{RT} = \frac{e}{k_B T}(V_{\text{cell}}^{\ominus} - V) - \bar{\mu} \tag{7}$$

with the applied voltage $V = \Phi_C - \Phi_A$ and diffusion potential $\bar{\mu}$. We re-write this expression in terms of overpotential

$$\eta = \frac{\tilde{\mu}_A - \tilde{\mu}_C}{e N_A} = V_{\text{cell}}^{\ominus} - V - \frac{k_B T}{e}\bar{\mu} \tag{8}$$

to compute the reaction massflux according to the classical Butler-Volmer equation [39]

$$j_N = j_0(x)\left(\exp\left(\alpha \frac{e\eta}{k_B T}\right) - \exp\left(-(1 - \alpha)\frac{e\eta}{k_B T}\right)\right) \tag{9}$$

where the exchange current density $j_0(x)$ is modelled as $j_0 = k_0\sqrt{x(1 - x)}$. We are aware of competing formulations [40, 41] but restrict our studies to this type of formulation. Inclusion of another exchange current density is, however, straightforward and can be studied with the code available in the Supplementary Material [42]. Results are shown exemplarily for the ACR-model in Appendix A. The rate constant k_0 and consequently j_N have dimensions [A/m²] and thus, the surface reaction is given by $R_{\text{surf}}(c,t) = j_N/F$ in [mol/(s m²)] with F being the Faraday constant. In the following, we assume symmetry of the reaction by setting $\alpha = 0.5$.

2.4. Boundary conditions

In simulations, we consider two cases, namely relaxation via spinodal decomposition under the assumption of a preceding non-equilibrium solid-solution pathway and, furthermore, galvanostatic charge and discharge. The first is captured by concentration conservation in the system while the second exhibits a flux across the electrode-electrolyte interface. The assumption of galvanostatic (dis-)charge can be modeled employing Eq. (9) on the surface while restricting the global flux (see [41])

$$I = \int_{\partial \mathcal{B}} \frac{1}{F} \boldsymbol{j} \cdot \boldsymbol{n} \mathrm{d}A \stackrel{!}{=} c_{\max} \, \text{C-rate} \int_{\mathcal{B}} 1 \mathrm{d}V \tag{10}$$

with dimensions [mol/s]. Eq. (10) can be utilized to compute the operating voltage V of our nanoparticle battery. The numerical procedure is sketched in the Supplementary Material [42].

2.5. Cahn-Hilliard model

The first model presented in this section stems from the works of Cahn and Hilliard [27, 28] and accounts for one chemical species with molar fraction c. The total free energy for a nonuniform system can, in first approximation, be expressed as

$$\mathcal{F}^{\mathrm{CH}}(c, \boldsymbol{\nabla} c) = \int_V f_{\mathrm{grad}}^{\mathrm{CH}}(\boldsymbol{\nabla} c) + f_{\mathrm{chem}}^{\mathrm{CH}}(c) \mathrm{d}V \tag{11}$$

consisting of two contributions, namely the gradient energy and the free chemical energy. The gradient energy penalizes the gradient of concentration

$$f_{\mathrm{grad}}^{\mathrm{CH}}(\boldsymbol{\nabla} c) = \boldsymbol{\nabla} c \cdot \boldsymbol{\kappa} \boldsymbol{\nabla} c \tag{12}$$

and features an ansiotropic parameter $\boldsymbol{\kappa}$ in the general case. For lithium iron phosphate as well as other cathode materials that exhibit a miscibility gap, the enthalpic term is usually modelled employing the simplest higher order Redlich-Kister term which leads to a symmetric free energy density with two distinct minima, also called regular solution

$$f_{\mathrm{chem,RS}}^{\mathrm{CH}}(c) = \frac{R}{V_m} T \big[c \ln(c) + (1-c) \ln(1-c) + \Omega c(1-c) \big] \tag{13}$$

where the parameter Ω is made dimensionless dividing by the thermodynamic pre-factor $RT c_{\max} = \frac{R}{V_m} T$ as we will consider constant temperature. The diffusion potential μ can be gained from the free energy by variation $\mu = \delta \mathcal{F}/\delta c$ and is the sum of two contributions

$$\begin{aligned} \mu &= \mu_{\mathrm{grad}} + \mu_{\mathrm{chem}} \\ &= -2\kappa \boldsymbol{\nabla}^2 c + \frac{\partial f_{\mathrm{chem}}^{\mathrm{CH}}(c)}{\partial c}. \end{aligned} \tag{14}$$

Inserting Eq. (14) into the reaction-diffusion equation (1) results in a fourth order PDE in c. The mobility function takes the form $\boldsymbol{M}(c) = \boldsymbol{D_0}c(1-c)/RTc_{\mathrm{max}}$ which leads to

$$\frac{\partial c}{\partial t} = \boldsymbol{\nabla} \cdot \left[D_0 c(1-c)\boldsymbol{\nabla}\big(\ln(c) - \ln(1-c) + \Omega(1-2c) - 2\kappa\boldsymbol{\nabla}^2 c\big)\right] + R(c,t). \tag{15}$$

The mass-conserving case without source term is typically referred to as *Cahn-Hilliard equation*. Considerable effort has been undertaken to include concentration-dependent eigenstrains and the corresponding elastic energy into this framework. Some works are formulated in the small deformation regime [10, 43–46] while others account for large deformations [47, 48]. Fracture mechanics has also been sucessfully coupled [46, 48]. Note that a simplified version of coherency strain is used for the 1D analysis in Sec. 3.2 assuming linear dependence of eigenstrains on the fluctuation of local concentrations with regard to the average composition. This results in an additional energy contribution quadratic in c while a more sophisticated treatment such as in the above-mentioned works is out of scope if this work.

2.6. Multi-phase field Allen-Cahn model formulation

For the sake of investigating polycrystalline samples, we furthermore employ a multiphase-field model based on the formulation presented in [6]. Following the notation in [14] we express the free energy functional in dependence of N phases with corresponding order parameters $\boldsymbol{\phi} = \{\phi_1, ..., \phi_\alpha, ..., \phi_N\}^T$ and K chemical species with molar fractions $\bar{\boldsymbol{c}} = \{\bar{c}_1, ..., \bar{c}_i, ..., \bar{c}_K\}^T$ as

$$\mathcal{F}(\boldsymbol{\phi}, \boldsymbol{\nabla}\boldsymbol{\phi}, \bar{\boldsymbol{c}}) = \mathcal{F}_{\mathrm{int}}(\boldsymbol{\phi}, \boldsymbol{\nabla}\boldsymbol{\phi}) + \mathcal{F}_{\mathrm{bulk}}(\boldsymbol{\phi}, \bar{\boldsymbol{c}}) \tag{16}$$

$$= \int_V f_{\mathrm{grad}}(\boldsymbol{\phi}, \boldsymbol{\nabla}\boldsymbol{\phi}) + f_{\mathrm{ob}}(\boldsymbol{\phi}) + f_{\mathrm{chem}}(\boldsymbol{\phi}, \bar{\boldsymbol{c}}) + f_{\mathrm{el}}(\boldsymbol{\phi}, \boldsymbol{\varepsilon})\mathrm{d}V, \tag{17}$$

consisting of interfacial and bulk contributions. The diffuse interface is determined by two terms, firstly the gradient energy density [49]

$$f_{\mathrm{grad}}(\boldsymbol{\nabla}\boldsymbol{\phi}) = -\varepsilon \sum_{\alpha, \beta > \alpha} \gamma_{\alpha\beta} \boldsymbol{\nabla}\phi_\alpha \boldsymbol{\nabla}\phi_\beta \tag{18}$$

with the numerical parameter ε linked to interface width and the interfacial energy $\gamma_{\alpha\beta}$ between two phases ϕ_α and ϕ_β. The second term f_{ob} is the multi-obstacle potential energy density

$$f_{\mathrm{ob}}(\boldsymbol{\phi}) = \frac{16}{\varepsilon\pi^2} \sum_{\alpha, \beta > \alpha}^{N} \gamma_{\alpha\beta} \phi_\alpha \phi_\beta \tag{19}$$

which, in combination with Eq. (18), prevents the non-physical formation of third phases in binary interfaces. The formulation allows to assign higher interfacial energies to the pre-existing grain/particle boundaries (as they are incoherent) than to the coherent FP-LFP interfaces that are formed during intercalation. The overall chemical energy is defined as the linear interpolation of phase-dependent energy terms $f_{\mathrm{chem}}(\boldsymbol{\phi}, \bar{\boldsymbol{c}}) = \sum f_{\mathrm{chem}}^\alpha(c^\alpha)\phi_\alpha$ with the volume fraction ϕ_α. The phase-dependent molar fractions $c^\alpha(\mu)$ are related by equal diffusional potential. The fitting functions of the phase-dependent chemical energies f_{chem}^α need to fulfill the

invertibility criterion [30] such that the chemical potential can be expressed as a function of molar fraction $\mu(c^\alpha)$. In this work, two formulations are used, namely the quadratric fit for computational efficiency and a logarithmic expression based on an ideal solution

$$f_{\text{quad}}^\alpha = A^\alpha(c^\alpha - c_{\min}^\alpha)^2 + B^\alpha, \tag{20}$$

$$f_{\text{ideal}}^\alpha = \mu_0^\alpha c^\alpha + K^\alpha c^\alpha \ln(c^\alpha) + K^\alpha(1 - c^\alpha)\ln(1 - c^\alpha) + B^\alpha. \tag{21}$$

The elastic energy contribution f_{el} including phase-dependent eigenstrains $\boldsymbol{\varepsilon}_\alpha^*$ is formulated as [50]

$$f_{\text{el}}(\boldsymbol{\phi}, \boldsymbol{\varepsilon}) = \frac{1}{2}[\boldsymbol{\varepsilon} - \boldsymbol{\varepsilon}^*] : \boldsymbol{\mathcal{C}}^{\text{eff}} : [\boldsymbol{\varepsilon} - \boldsymbol{\varepsilon}^*] \tag{22}$$

assuming linear interpolation of stiffnesses $\boldsymbol{\mathcal{C}}^{\text{eff}} = \sum \boldsymbol{\mathcal{C}}_\alpha \phi_\alpha$ and linear interpolation of eigenstrains $\boldsymbol{\varepsilon}^* = \sum \boldsymbol{\varepsilon}_\alpha^* \phi_\alpha$. A discussion regarding this choice of interpolation coupled with chemcial driving forces can be found in [51, 52].

Evolution of order parameters is computed as the summation of dual interactions [9]

$$\frac{\partial \phi_\alpha}{\partial t} = -\frac{1}{\tilde{N}\varepsilon}\sum_{\beta \neq \alpha}^{\tilde{N}} M_{\alpha\beta}\left[\frac{\delta\mathcal{F}_{\text{int}}}{\delta\phi_\alpha} - \frac{\delta\mathcal{F}_{\text{int}}}{\delta\phi_\beta} + \frac{8}{\pi}\sqrt{\phi_\alpha\phi_\beta}\Delta^{\alpha\beta}\right] \tag{23}$$

where we use the abbreviation $\Delta^{\alpha\beta} = \delta\mathcal{F}_{\text{bulk}}/\delta\phi_\alpha - \delta\mathcal{F}_{\text{bulk}}/\delta\phi_\beta$. $\tilde{N} \leq N$ is the number of locally active phases and $M_{\alpha\beta}$ denotes the mobility of an α-β interface. This choice is motivated by the interpolation function that ensures the correct traveling wave solution for a binary interface $h_{\text{ob}}(\phi) = \frac{1}{2} + \frac{2}{\pi}\left((2\phi - 1)\sqrt{\phi(1 - \phi)} + \frac{1}{2}\arcsin(2\phi - 1)\right)$. The derivative of this interpolation function $\partial h_{\text{ob}}(\phi)/\partial\phi = \frac{8}{\pi}\sqrt{\phi(1 - \phi)}$ is then generalized for the multi-phase case. Note that this formulation is no longer fully variational.

The composition evolution is given by a set of reaction-diffusion equations for $K-1$ independent components driven by the diffusion potentials μ_j

$$\frac{\partial\bar{c}_i}{\partial t} = \boldsymbol{\nabla}\cdot\left(\sum_{j=1}^{K-1}\bar{\mathcal{M}}_{ij}(\boldsymbol{\phi})\boldsymbol{\nabla}\mu_j\right) + R_i. \tag{24}$$

The mean mobility comprises the individual phase mobilities $\bar{\mathcal{M}}_{ij} = \sum_\alpha^N \mathcal{M}_{ij}^\alpha \phi_\alpha$ where each $\mathcal{M}_{ij}^\alpha$ is defined by $\mathcal{M}_{ij}^\alpha = D_{ij}^\alpha \partial c_i^\alpha/\partial\mu_j$ in the general case. We rewrite evolution equation (24) in terms of diffusional potential following [30]. From $\bar{c}_i = \sum_\alpha^N c_i^\alpha \phi_\alpha$ we derive

$$\frac{\partial\bar{c}_i}{\partial t} = \sum_\alpha^N \frac{\partial c_i^\alpha}{\partial\mu_k}\frac{\partial\mu_k}{\partial t}\phi_\alpha + \sum_\alpha^N c_i^\alpha\frac{\partial\phi_\alpha}{\partial t} \tag{25}$$

and thus obtain the evolution equation for diffusional potentials [30]

$$\frac{\partial\mu_k}{\partial t} = \left[\sum_\alpha^N \frac{\partial c_i^\alpha}{\partial\mu_k}\phi_\alpha\right]^{-1}\left[\boldsymbol{\nabla}\cdot\left(\sum_{j=1}^{K-1}\bar{\mathcal{M}}_{ij}(\boldsymbol{\phi})\boldsymbol{\nabla}\mu_j\right) + R_i - \sum_\alpha^N c_i^\alpha\frac{\partial\phi_\alpha}{\partial t}\right]. \tag{26}$$

Since stress evolution is assumed to be orders of magnitude faster compared to diffusional processes, we solve for static mechnical equilibrium

$$\boldsymbol{\nabla} \cdot \boldsymbol{\sigma} = 0. \tag{27}$$

Stresses are computed based on the generalized Hook's law $\boldsymbol{\sigma} = \boldsymbol{\mathcal{C}}^{\text{eff}} : [\boldsymbol{\varepsilon} - \boldsymbol{\varepsilon}^*]$ where we implicitly introduce additive superposition of strains in the small deformation regime. Total strains are defined as the symmetric part of the displacement gradient $\boldsymbol{\varepsilon} = \frac{1}{2}(\boldsymbol{\nabla u} + (\boldsymbol{\nabla u})^{\text{T}})$.

2.7. Comparison of the two approaches

The modeling of intercalation compounds has traditionally been based on the Cahn-Hilliard formulation presented in Sec. 2.5 (see [25, 26, 53]) which poses the numerical challenge to solve for a fourth-order PDE. The model in Sec. 2.6 on the other hand, is composed of coupled second-order conservative and non-conservative equations [30, 37, 54]. We compute the evolution of order parameters, which are non-conserved via the Allen-Cahn equation (23), and secondly the evolution of chemical potential (26), which is based on mass conservation. This modeling approach now changes the perspective by actively distiguishing between high and low composition regions by individual order parameters. This allows us to drop the gradient term in composition such that interfaces are solely defined by the transition of order parameters in a diffuse interface region with finite length. Furthermore, interface characteristics as the interfacial energy $\gamma_{\alpha\beta}$ and interfacial width $L(\varepsilon)$ become independent from bulk contributions. In this picture, each phase has its own ideal-solution-like free energy while the enthalpic term of species interaction, that leads to a miscibility gap, is imposed by the obstacle potential. This term can be interpreted as an additional phase-mixture contribution which represents the activation energy to be overcome for phase transformation. For a two-phase case we could write the generic expression [55]

$$f_{\alpha\beta} = \phi f_\alpha(c^\alpha) + (1 - \phi) f_\beta(c^\beta) + \Delta f_{\text{phmix},\alpha\beta} \tag{28}$$

with the phase-mixture contribution $\Delta f_{\text{phmix},\alpha\beta}$. In this study the double-obstacle potential Eq. (19) is employed. In our previous work [6], we outlined how conventional parameters such as interfacial energies and width can be related and, additionally, showed that the instability limits for nucleation of new phases can be matched. However, the two modeling approaches exhibit different kinetics with regard to nucleation and phase separation which will partly be discussed in the remainder of the paper.

2.8. Material data for LiFePO₄

The charge and discharge of $LiFePO_4$ is accompanied by a first-order phase tranformation $FePO_4 \rightarrow LiFePO_4$ between lithium-rich and poor olivine phases exhibiting a large miscibility gap [1]. This leads to a voltage plateau of the open circuit voltage at 3.422V measured against pure metal anode with a residual voltage gap of about 10mV, even after very slow cycling with $C/1000$ [38]. The lattice constants a, b and c of

both phases given Tab. 1 have been measured in various experimental works [1, 56] with very low variation. Normal eigenstrains ε^0 along the primary crystal axes can be calculated as $\varepsilon_a^0 = (a_{\text{LFP}} - a_{\text{FP}})/a_{\text{FP}}$ and are given in Tab. 1. The calculated normal strains are equivalent to the values used in other works [25, 57]

Table 1: Phase characteristics taken from [56]

Parameter		FePO$_4$	LiFePO$_4$	ε^0
Lattice	a	9.826	10.334	5.2%
constants	b	5.794	6.002	3.6%
in Å	c	4.784	4.695	−1.9%

and are strongly direction-dependent. The orthorombic olivine structure of LiFePO$_4$ is anisotropic in many more properties such as diffusion, surface energies, elastic constants and surface redox potentials. Elastic constants can be gained from DFT calculations and we take the values according to the GGA+U from [18]. Surface energies are also highly anisotropic and can be computed from DFT simulations [58, 59]. The corresponding Wulff shape shows a crystal with large (010) facets for both FP and LFP (see Supplementary Material [42]). This result is consistent with the nano-platelets gained by hydrothermal synthesis [56, 60]. When phase separation occurs in an Li$_X$FePO$_4$ particle with average composition X, an intra-particle interface is present. The energy penalty for this event is given by the combination of chemical intefacial energy $\gamma_{\text{LFP-FP}}$ scaled by interfacial area and the coherency strain accomodated across the particle. The latter is highly dependent on the boundary condition. The chemical interfacial energies for an LFP-FP interface have been computed via DFT [19] and are given in Tab. 2. The interplay of anisotropies plays a

Table 2: Interface energies of LFP-FP interface [19]

Orientation	(100)	(010)	(001)
$\gamma_{\text{LFP-FP}}$ in [J/m^2]	0.115	0.007	0.095

significant role on the formation of phase separation, especially as they scale differently with particle size. Regimes where different interfaces are energetically favourable can be predicted.

Diffusion is confined to 1D channels along the b-axis, which has been shown experimentally [56] and through theoretical calculations [17]. The diffusion anisotropy varies with defect concentration and is, therefore, size-dependent. Under the assumption that the diffusivities scale similarly with temperature in all three directions, we use the values at an average defect concentration of $\rho_{\text{defect}} = 0.05$ (and show them for $\rho_{\text{defect}} = 0.005$ for comparison in Tab. 3).

Table 3: Li-vacancy self diffusion coefficient D_{Li} at $T = 300K$ [17] given in $[\mathrm{m}^2/\mathrm{s}]$

ρ_{defect}	$= 0.005$	$= 0.05$
(100)-direction	$3.9 \cdot 10^{-18}$	$3.9 \cdot 10^{-17}$
(010)-direction	$1.3 \cdot 10^{-14}$	$1.3 \cdot 10^{-15}$
(001)-direction	$7.8 \cdot 10^{-19}$	$7.8 \cdot 10^{-18}$

2.9. Modeling assumptions

For the sake of simplicity, the models have been formulated under various assumptions with respect to generality of geometry and parameter space. Hence, drawn conclusions from the simulations may only be valid under the posed assumptions. In the simplest case we investigate a cathode which consists of only one particle which is equivalent to the assumption of many particles that undergo the exact same process simultaneously. We start from the assumption of a platelet-like morphology and conduct two types of simulations:

- **Bulk kinetics:** We investigate the relaxation into the phase-separated state from a solid solution (i.e. spinodal decomposition) which captures the physics of quenching experiments like [61]. This scenario is rather academic but yields valuable insight into the bulk diffusion behaviour decoupled from the effects of electro-chemical reaction. This allows us to test the validity of the phase-field model including strongly anisotropic mobilities and surface enegies. Effects on the nanoscale are captured and discussed to motivate the dimensionality reduction for the following simulations.

- **Charge and discharge:** Charging a battery with constant current is a typical use-case. The applied overpotential and possible phase tranformations are highly dependent on the morphology of primary particles or agglomerates as well as possible diffusion pathways.

Following [56], only the ac-plane is active for Li extraction and insertion in our simulations. The interface between FP and LFP is assumed to be coherent [25] and, thus, should have an interfacial energy lower than $0.2\,\mathrm{J/m}$ [10]. We therefore employ the values presented in Tab. 2. For the CH-model, the gradient energy parameter $\boldsymbol{\kappa}$ is also direction-dependent and is fitted to reproduce the chemical interface energies given in Tab. 2. The maximal concentration of intercalated ions $c_{\max} = 22809\,[\mathrm{mol/m}^3]$ is computed from the lattice parameters in Tab. 1 and accounts for four intercalation sites per unit cell. The enthalpy of mixing $\Omega = 0.115\,e\mathrm{V/Li}$ is taken from Cogswell *et al.* [10]. The following sections are motivated by the following research questions: Which minimal model is suitable to describe ion intercalation in phase-separating electrode materials and can be included in Newman-type modeling approaches? Which are the dominant processes driving phase separation in intercalation compounds that should therefore be accounted for?

12

3. Results and discussion

3.1. Dimensionality reduction

Dimensionality reduction affects the overall model formulation as the results are heavily influenced by the underlying assumptions. First, we discuss various modeling approaches in one dimension because this type of reduced model is often used in the context of porous electrode modeling (e.g. P2D models like MPET [62]). Typical ways to reduce dimensionality are sketched in Fig. 2. The assumption of a particle with spherical symmetry in Fig. 2a is quite common in P2D models, but has to be treated with care for materials undergoing phase transformations as it tacitly introduces the notion of a core-shell structure. In a chemo-mechanical model, this automatically leads to high hoop stresses for phase separation during charge and discharge if there is a lattice mismatch between ion-rich and ion-poor phases. Furthermore, material parameters are assumed to be isotropic due to the symmetry condition. The core-shell structure and material isotropy are contradictory to experiments and the known material parameters, especially for highly anisotropic materials such as $LiFePO_4$, which is discussed here.

(a) 1D spherical particle   (b) 1D slab   (c) 1D thin crystal
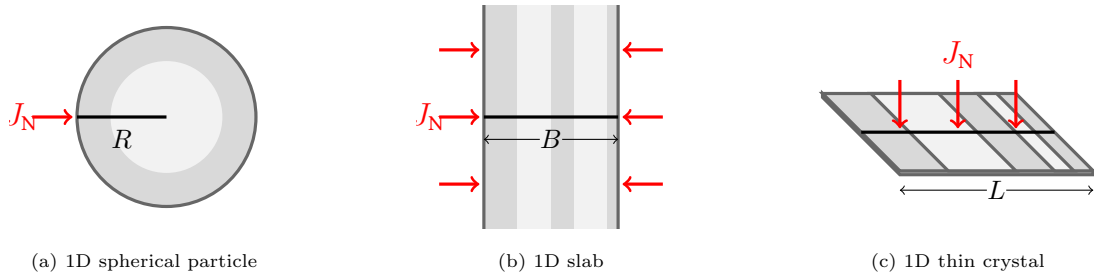
Figure 2: Simulation setup for particle intercalation study.

The 1D slab approach in Fig. 2b assumes a finite width B but infinite extension in the other two dimensions. Phase separation occurs as moving planar fronts along the cross-section of the slab. Different directions in the crystal lattice can be investigated in an isolated manner, which allows anisotropies to be studied to some extent. Mechanical stresses are expected to be highly overestimated as the boundary conditions (1D equivalent to plane strain) do not allow for stress relaxation in the tranverse directions. The third approach in Fig. 2c is different in the sense that it reduces one dimension by symmetry and the other by volume averaging. The ion composition is averaged in the thin dimension (assuming fast diffusion and filling in that direction) and another dimension is again reduced assuming infinite extension of the plate. The surface flux then turns into a volume source term. Mechanical stresses can be expected to be more realistic as the thin dimension is assumed to be a stress-free surface, thus allowing for some stress relaxation. The correct choice of a reduced model is material specific and should reflect the dominant material anisotropies. A comparison between the different options can be carried out e.g. with the open-source framework MPET [62] which includes the geometries sketched in Fig. 2 and, furthermore covers phase-separation.

13

3.2. Bulk kinetics

In their review, Malik *et al.* [4] come to the conclusion that there are three relevant length-scales that need to be considered to accurately model the kinetics in LFP, namely the bulk, the single-particle and multi-particle scales. In this section, we start off with bulk diffusion on the nano-scale to draw first conclusions which are relevant for modeling of the other two scales. The Cahn-Hilliard model presented in Sec. 2.5 naturally describes the process of phase separation by diffusion well within the spinodal region, which is why we employ this model throughout this section. Starting from a solid solution with some random fluctuations, we conduct relaxation simulations in three possible 2D cross-cuts, shown in Fig. 3. We employ no-flux boundaries and neglect all surface effects at the electrolyte interface. The respective third dimension is reduced assuming symmetry such that the relaxation within planes can be investigated in an isolated manner. The results in
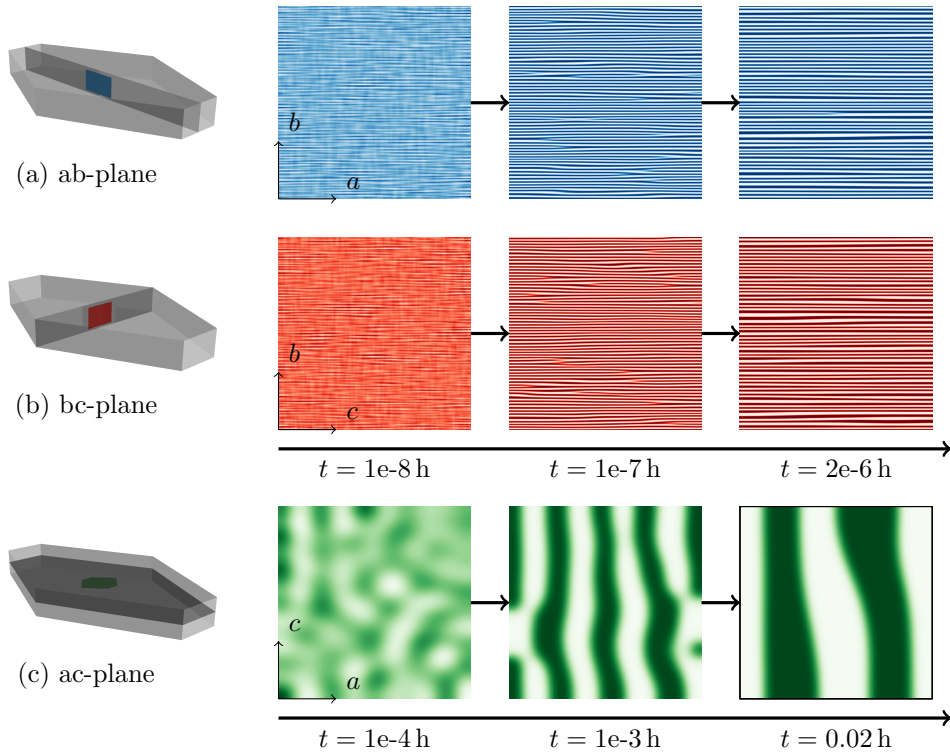
Figure 3: Virtual quenching experiment with relaxation from solid solution with $c_{\mathrm{init}} = 0.5$ in $50 \times 50\,\mathrm{nm}$ 2D cross-sections. Three timesteps of temporal evolution are shown for (a) the ab-plane, (b) the bc-plane and (c) ac-plane. Both simulations including the b-axis show phase separation on much smaller spatial and time scales compared to the ac-plane. All simulations assume symmetry (infinite extension) in the third dimension and have no-flux boundaries.

Fig. 3 suggest that the fastest and thus preferred path to reduce the overall energy in the system is phase separation along the b-axis which leads to very fine striping. The wavelength of fluctuations is in the order of lattice parameters and the predicted interfacial width in the b-direction is $l_{010} = 1.96 \cdot 10^{-10}\,\mathrm{m}$. The spatial scale of striping is below the optical resolution of many experimental works such that the composition would

14

appear homogenous. These simulations qualitatively agree with the finding that there are ordered states of alternating filled and empty ac-planes that minimize the overall energy in comparison with a disordered solid solution [22, 63]. Further reduction of interfacial energies by coarsening of the striped pattern would lead to an ac-interface between lithium-rich and -poor phases over time as has been observed in quenching experiments by Chen *et al.* [61]. The two main reasons for this behaviour are the comparatively small interfacial energy in the b-direction combined with the mobility of ions which is orders of magnitudes higher within the (010)-channels. It should be noted that it is difficult to quantitatively match the reduced energy states for ac-ordering presented in [63] with phase-field simulations. Energy values strongly depend on the free energy function and in this specific case on the choice of the enthalpy of mixing Ω for the regular solution. The formation energies calculated with DFT refer to $0\,\mathrm{K}$ but simple superposition with an ideal solution as in Eq. (5) does not reproduce the experimentally observed miscibility gap.

The dynamics of spinodal decomposition in the early stage can be derived using Fourier analysis of fluctuations in the initial solution [64]. The derivations only hold for the one-dimensional case and $\int (c - c_0)\mathrm{d}x = 0$ which basically implies a closed system with no-flux BCs. For a fluctuation of the form $(c - c_0) = A\cos(\frac{2\pi}{\lambda}x)$, we can derive the critical and maximum wavenumber

$$\beta_c = \frac{2\pi}{\lambda_c} = \sqrt{\frac{-\partial^2 f/\partial c^2}{2\kappa}}, \quad \beta_{\max} = \beta_c/\sqrt{2}.$$

To estimate the influence of coherency strain on the resulting pattern formation, we add another free energy contribution $f_{\mathrm{el}}^{\mathrm{CH}}(c)$ to our analysis. Coherency strain due to a change in molar volume is introduced assuming linear dependence of the eigenstrain on the local composition fluctuation $c - c_0$ for orthotropic material properties (which is a generalization of the isotropic case in [28])

$$f_{\mathrm{el}}^{\mathrm{CH}}(c) = \frac{1}{2}\boldsymbol{\sigma} : [\boldsymbol{\varepsilon} - \boldsymbol{\varepsilon}^*] = \frac{1}{2}\Psi(\boldsymbol{n})(c - c_0)^2. \tag{29}$$

The direction-dependent parameter $\Psi(\boldsymbol{n})$ is derived in the Supplementary Material [42] assuming a 1D slab with free ends but infinite extension in the transverse directions (1D equivalent of plain strain). For the three-dimensional case, the more general case should be used by solving for static momentum balance $\boldsymbol{\nabla} \cdot \boldsymbol{\sigma} = \boldsymbol{0}$. The second derivative of energy densities with respect to c then reads

$$\frac{\partial^2 f}{\partial c^2} = \frac{1}{c_0(1 - c_0)} - 2\Omega + \Psi \tag{30}$$

for the initial case of negligibly small $\boldsymbol{\nabla}c$. From this and the evolution Eq. (1), the exponential factor describing the rate of fluctuation growth $(c - c_0) = \exp[R(\beta)t]\cos(\beta x)$ can be computed depending on the

15

initial concentration c_0 and corresponds to the wavelength of the fastest growing unstable fluctuation $\lambda^{\max}$

$$R_{\max}(c_0) = M\frac{(\partial^2 f/\partial c^2)^2}{8\kappa}$$

$$= \frac{Dc_0(1-c_0)}{8\kappa}\left(\frac{\partial^2 f}{\partial c^2}\right)^2\bigg|_{c_0} \tag{31}$$

$$\lambda^{\max}(c_0) = \frac{2\pi}{\beta_{\max}} = \frac{4\pi\sqrt{\kappa}}{\sqrt{2\Omega - \Psi - \frac{1}{c_0(1-c_0)}}}. \tag{32}$$

Inserting the values for LiFePO$_4$, we compute the amplification factors for the purely chemical case, where $f = f_{\text{chem}}^{\text{CH}}$, and for the coupled case accounting for coherency strains $f = f_{\text{chem}}^{\text{CH}} + f_{\text{el}}^{\text{CH}}$. The results are plotted in Fig. 4.
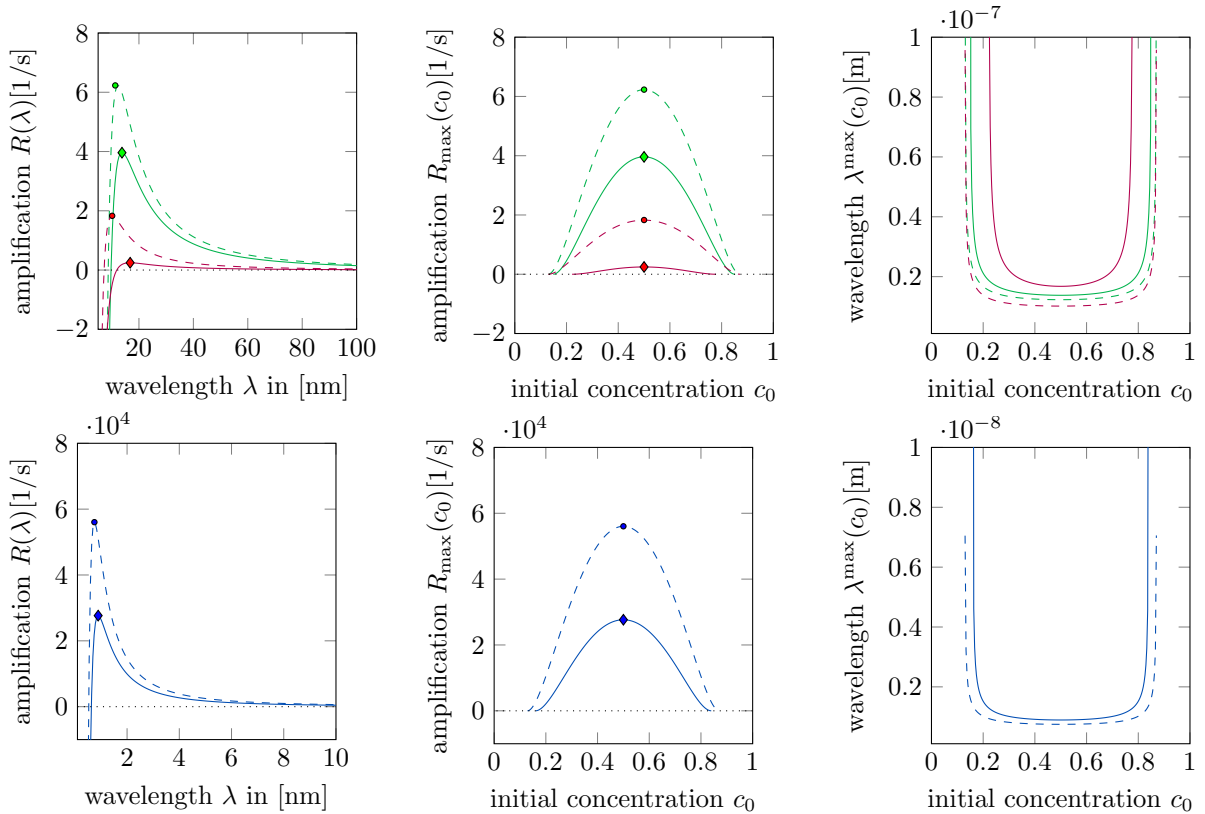
Figure 4: Amplification factors for unstable fluctuations in the (100)-direction shown in green and in the (001)-direction shown in red in the top row. Unstable fluctuation in the (010)-direction are shown in the bottom row in blue. The dashed lines represent the purely chemical case while the solid curves include the additional influence of coherency strain. The left graph shows the amplification factor depending on the wavelength of the fluctuation for $c_{\text{init}} = 0.5$. The central graph shows the maximal amplification $R_{\max}$ (as marked in the left graph) for every $c_{\text{init}} \in [0, 1]$. On the right, the corresponding wavelengths are plotted.

Generally, we observe negative $R(\lambda)$ for very small wavelengths (which means cancellation), while between the critical wavelengths all fluctuations are amplified. The amplification factor features a distinct peak at

16

λ^{max}, indicating that we expect phase separation within a small interval of wavelengths around the peak value. The visualization of $R_{\mathrm{max}}(c_0)$ in the central graphs of Fig 4 reveals two more details. First, the overall maximal amplification can be found for $c_{\mathrm{init}} = 0.5$ due to the symmetry of f. Secondly, amplification tends towards zero as the initial composition approaches the spinodal. This has been discussed by Cahn [28] and implies that this model cannot describe nucleation as it does not allow for growth of small but finite fluctuations i.e. nuclei. The comparison of lattice directions (100) and (001) clearly shows that amplification factors are higher along the a-axis. In both cases, coherency strain delays phase separation by reducing the amplification factors. Additionally, there is a small shift of the maximal amplification towards higher wavelength as can be seen in the left graphs for $c_{\mathrm{init}} = 0.5$ and for all $c_{\mathrm{init}} \in [0, 1]$ in the right subfigure of Fig. 4. Applying the same analysis to the b-axis reveals that the spatial scale as well as the time scales differ drastically. While the exponential growth of fluctuations in the a-axis is in the order of $1/R_{\mathrm{max}} = 1\,\mathrm{s}$, the predicted phase separation along the b-axis is in the order of $10^{-4}\,\mathrm{s}$. Furthermore, much smaller fluctuations are excited, leading to expected wavelengths smaller than $1\,\mathrm{nm}$ which is in the order of the lattice parameters (compare Tab. 1).

The mechanical contribution generally reduces the amplification of phase separation and in the specific case of the b-direction by a factor of 2.0. However, this reduced value is still four orders of magnitude larger compared to the other two directions which means that even with inclusion of coherency strain, ordered states and phase separation in the b-direction will be observed. We conclude that diffusion kinetics has a strong influence on the resulting pattern formation. Quantative phase-field modeling that resolves this smallest scale needs to reflect the strong anisotropies of diffusion, interfacial energies and stiffness to yield meaningful results. Results obtained under the assumption of isotropy, which can either be introduced implicitely by spherical symmetry (see Fig. 2a) or explicitly by using a scalar value for the gradient parameter κ, are highly questionable. From a numerical point of view, the strong anisotropy of LFP poses a severe challenge for simulation studies. The small spatial scale of striping limits the overall accessible time and length scales to such an extent that simulation of full or half cycles with technically relevant C-rates becomes infeasible with our code. Furthermore, the chosen simulation setup only captures bulk effects, while the inclusion of surface energy effects at the particle-electrolyte interface is likely to alter the observed phase separation [44]. Surface diffusion and ion exchange with the electrolyte at zero net current enable diffusion across the b-channels which could promote faster phase separation at the particle surface. These could be the thermodynamic reasons for the observation that $\mathrm{LiFePO_4}$ forms at the surface while a solid-solution remains within the particle for quenching of $\mathrm{Li}_X\mathrm{FePO_4}$ with $X > 0.6$ [61].

The remaining question is: How can homogenization be applied to access larger time and length scales using the phase-field method? We argue that the results in Fig. 3 could be interpreted as a solid solution with ordering, coinciding with the results in [22, 63, 65]. The effective, homogenized free energy landscape should be altered compared to the case of a disordered solid solution. However, the phase-field model fails to predict

an effective mobility of ions because of its continuum assumptions regarding Fickian diffusion for an ideal solution. A quantitative homogenization should be the goal of future investigations and we are confident that this issue can be addressed by a collaboration of phase-field and KMC methods [22, 23]. While micron-sized particles are likely to be dominated by diffusion limitations [66] and stress effects [67], intermediate solid-solution states have been observed in nano-sized platelets at technically relevant C-rates [65]. This observation motivates homogenization by depth-averaging in the b-direction for thin platelets as sketched in Fig. 2c. Not resolving the atomistic length scale, we neglect ordering effects and phase separation in the 010-direction and replace the local composition variable $c(x, y, z, t)$ with the averaged $\bar{c}(x, y, t) = 1/H \int c(x, y, z, t) \mathrm{d}z$ [5]. This simplification is the basis for the simulation studies in the following section.

3.3. Galvanostatic charge and discharge

Based on the assumptions that, first, only (010)-facets are active for the electro-chemical insertion reaction [56] and secondly, that phase boundary migration progresses according to the domino cascade mechanism [68], the depth-averaged model sketched in Fig. 2c has been formulated [5]. In combination with the boundary condition of galvanostatic (dis-)charge in Sec. 2.4, we end up with a reaction diffusion model as in Eq. (1). Due to the depth-averaging, the surface flux turns into a bulk source term $R(c, t)$ with local dependence on filling fraction. There are two possible assumptions for the in-plane diffusion of intercalated ions, namely

- The limit of $D_{\mathrm{Li}}^{(100)} \to 0$ and $D_{\mathrm{Li}}^{(001)} \to 0$ describes a perfect crystal where diffusion is confined to 1D channels along the b-axis. The model reduces to a reaction equation in the ac-plane, which is why this model has been called *Allen-Cahn-reaction model* (ACR model) [5, 40].

- The presence of crystal defects lowers the diffusivity in the b-direction and furthermore allows for diffusion in the ac-plane. The underlying model is a reaction-diffusion equation and can be computed employing the diffusivities in Tab. 3 for various defect concentrations. Accounting for surface diffusion, leads to the same evolution equation for ion composition [69]. So in the general sense, the diffusivity in the depth-averaged model could be interpreted as the effective in-plane diffusivity combining bulk and surface effects.

Both cases are simulated and compared in the following. We use a reference cell voltage of $V_{\mathrm{cell}}^{\ominus} = 3.422\,\mathrm{V}$ and the pre-factor $k_0 = 10^{-2}$ for the Butler-Volmer equation [70] if not stated otherwise. Starting from an initially homogenous filling fraction of $c_{\mathrm{init}} = 0.01$ including some random noise with amplitude $A = 0.001$ to account for thermal fluctuations, several C-rates are applied to study the coupled effects of reaction and diffusion. Coherency strains are neglected in this section.

We start with the ACR model and apply C-rates $C = 2^N\,[1/\mathrm{h}]$ where $N \in [-6, -5, ..., 2]$. The results in Fig. 5 imply that phase separation (which is characterized by a plateau in the voltage plot and a high
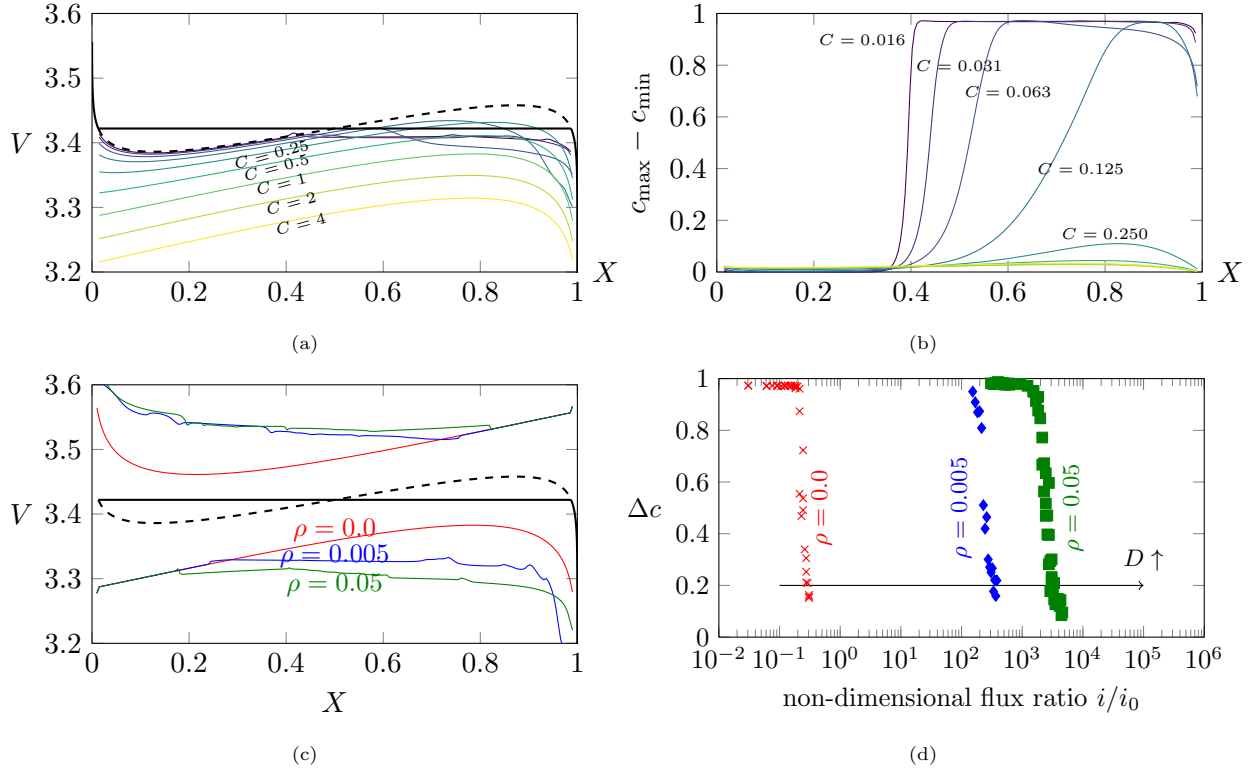
Figure 5: Rate-dependent charging behaviour obtained with the Cahn-Hilliard approach (Sec. 2.5). In a) the operating voltage V over Li content X in $\mathrm{Li}_X\mathrm{FePO}_4$ is shown for boundary conditions according to Eq. (10) with varying C-rate $C = 2^N\,[1/\mathrm{h}]$ where $N \in [-6, -5, ..., 2]$ and a constant thickness of $H = 50\,\mathrm{nm}$. The equilibrium case is drawn in black according to Eq. (6). The maximal concentration difference over time is shown in b) indicating a transition from phase separation to solid solution around $C = 0.1$. The influence of in-plane diffusion on phase separation is added in c) and d). For C-rate= 1 and defect concentrations $\rho_{\mathrm{defect}} = \{0.0, 0.005, 0.05\}$ the voltage profile V is shown in c). The maximal occuring composition difference $\Delta c = \max(c_{\max} - c_{\min})$ over the non-dimensional flux ratio is given in d) illustrating the transition to solid solution behaviour depending on ρ.

composition difference $c_{\max} - c_{\min}$ in the domain) can be suppressed for high currents. In the present case, the limit lies around C-rate= 0.1, but it should be noted that this value is highly dependent on the choice of the parameters k_0 and the thickness H of the depth-averaged crystal. The critical current to suppress phase separation can be expressed more generally by means of the non-dimensional flux ratio

$$\frac{i}{i_0} = \frac{I}{A_{\mathrm{reac}}i_0} = \frac{\text{C-rate} \times H \times F \times c_{\max}}{2k_0}, \tag{33}$$

where I denotes the total flux according to Eq. (10) in [mol/s] and A_{reac} is the active surface area (in this case $2LB$). The averaged reaction flux is scaled to the characteristic reaction flux $i_0 = k_0/F$ which is a material surface property. If we allow for bulk diffusion in the simulated plane, the stability limit to suppression of phase separation changes drastically. This can be seen by comparison of the hysteresis for C-rate=1 in Fig. 5c. While the assumption of a perfect crystal (ACR limit) predicts suppression of phase

19

separation, the other two cases with assumed defect concentrations of $\rho_{\mathrm{defect}} = 0.005$ and $\rho_{\mathrm{defect}} = 0.05$ exhibit large voltage plateaus caused by the two-phase coexistence. There can still be suppression of phase separation but it shifts to higher C-rates (i.e. higher non-dimensional flux ratios) if in-plane ion transport is possible.

The depth-average assumption enforces the same electro-chemical potential in the bulk as on the surface of the active facets, which is why the dynamic suppression of phase separation at high charging rates is very sensitive to the free energy formulation. Employing the experimentally motivated energy fits shown in Fig. 1b will consequently alter the onset of phase separation. Another significant difference between the two modelling approaches outlined in Sec. 2.5 and 2.6 is that within the multi-phase field approach, the phase transition from FP to LFP is modelled as a first-order transformation while the Cahn Hilliard model describes the change of composition as a second-order transformation. As a consequence, the LFP phase occurs once an energetic barrier imposed by the obstacle potential is overcome which is independent of the charging rate. This is confirmed by the results in Fig. 6a in which the onset of the first-order phase transformation is initiated at the same average composition but then proceeds at different speeds depending on the imposed charging rate.
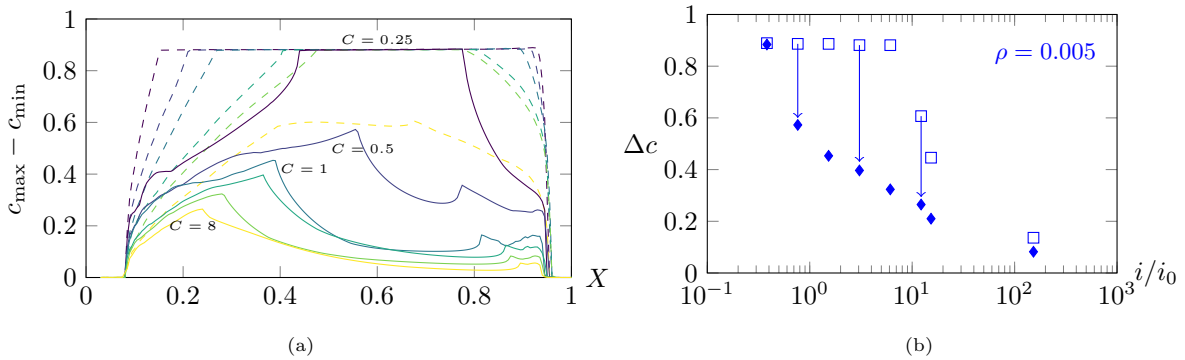

(a)

(b)

Figure 6: Rate-dependent phase separation upon discharge obtained with the multi-phase approach (Sec. 2.6). The maximal concentration difference over average filling fraction X in $\mathrm{Li}_X \mathrm{FePO}_4$ is shown in a) for varying C-rate $C \in [0.25, 0.5, 1, 2, 4, 8]\, 1/\mathrm{h}$ and a constant thickness of $H = 50\,\mathrm{nm}$. Dashed lines denote simulation neglecting the influence of coherency strain while solid lines include elastic deformation. The effect of in-plane diffusion with assumed defect concentration $\rho_{\mathrm{defect}} = 0.005$ is included. The maximal occuring composition difference $\Delta c = \max(c_{\mathrm{max}} - c_{\mathrm{min}})$ over the non-dimensional flux ratio is given in b) illustrating the transition to solid solution behaviour depending on elastic energy and C-rate. Square symbols represent simulations without elasticity and diamonds show simulations including the influence of elastic deformation.

Another important factor that alters the observed phase separation is the inclusion of coherency strain. The stored elastic energy due to lattice mismatch changes the energetic equilibrium by penalizing phase separation which is different from the dynamic competition of surface reaction and in-plane diffusion. As can be seen in Fig. 6 and Fig. 7, a complete demixing into areas of FP and LFP becomes unfavourable while intermediate composition states are promoted. Note that in this study we assumed traction free

boundaries such that the nano-particle can expand freely. As a result, only internal stresses arise due to phase separation within the computational domain. The evolution of composition and coupled principle stresses is shown exemplarily for a C-rate of 0.25 at a low defect concentration of $\rho = 0.005$ in Fig. 7. Due to the influence of coherency strain, larger areas of an intermediate composition form and buffer the lattice mismatch between the end-member phases FP and LFP. Interfaces tend to align with the {101} family of crystal planes to reduce the stored elastic energy [10]. Areas with lower Li content exhibit higher tensile stresses due to the overall lattice strain. In the bottom row of Fig. 7, we display the maximal local tensile stresses as this is the relevant stress measure for fracture in brittle materials.
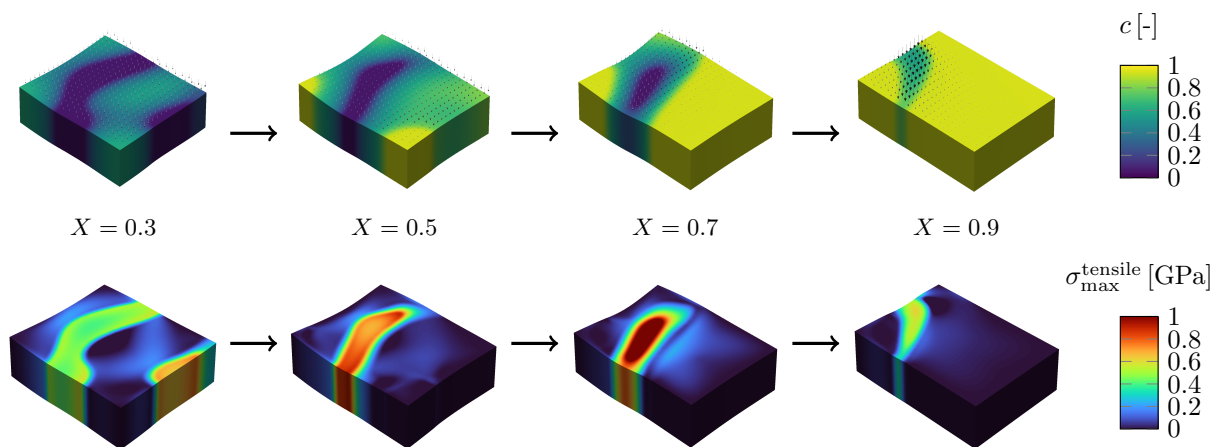
Figure 7: Discharge simulation of a thin platelet with dimensions $50 \times 50\,\text{nm}$ under the depth-average assumption using the multi-phase approach including coherency strain. X denotes the average filling fraction in Li_XFePO_4 while the local composition c is indicated by the green color scale in the top row. The arrows indicate the magnitude of reaction flux vectors and illustrate how the reaction flux intensity follows the front of phase transformation. The bottom row shows the maximum principle stress in GPa. Stresses and strains are computed fully 3D and at all surfaces we apply homogenous Neumann boundary conditions. Displacements resulting from lattice expansion are superposed with a magnification of 5.

Generally, as soon as phase separation occurs, the reaction flux becomes highly non-homogenous across the domain. It can easily be shown that the formulation of the Butler-Volmer equation Eq. (9) favours electrochemical reaction at the phase boundaries between high and low concentration phases [11, 71]. This is also observed in all (dis-)charge simulations exhibiting phase separation and shown exemplarily in Fig. 7. Starting from a homogenous flux distribution inside the domain, the flux then concentrates on the interfacial areas as soon as phase separation occurs. The reaction flux intensity follows the phase fronts as the particle gets filled. In this sense, the suppression of phase separation is not only favourable to avoid high tensile stresses, which likely promote mechanical degradation, but it also leads to a more homogenous flux distribution across the active facet reducing the probability of parasitic side reactions due to high local fluxes and overpotentials. These results illustrate the importance of correct modeling of the electro-chemical reaction at the electrode-

electrolyte interface. The assumption of constant flux (locally- as opposed to globally-constant flux which reflects the CC charge) is only valid for non-phase-separated states and small concentration gradients on the surface. Furthermore, it is compliant with the 1D spherical model (see Fig. 2a) as the prescribed shrinking core features the same surface concentration.

3.4. Multigrain systems

The simulations in the previous sections shed some light on the possible phase transformations and the interplay of electro-chemo-mechanical forces in single crystals. The obtained voltage curves are valid in the limit of a single particle getting charged or many particles undergoing the exact same process. The actual multi-particle behaviour in battery electrodes is, however, much more complicated. In a multi-particle system, the state of charge does not necessarily coincide with the average composition in each particle. Instead, there are many thermodynamic states that minimize energy and the actual ion distribution is history-dependent [4]. It is energetically favourable for the phase transition $FePO_4 \rightarrow LiFePO_4$ to proceed in a particle-by-particle manner, i.e. to have inter-particle instead of intra-particle phase separation [68, 72], sometimes referred to as mosaic pattern [72]. This fact also leads to the non-vanishing hysteresis in the limit of C-rate$\rightarrow 0$ [38]. LFP is mostly produced as single crystals and phase-field simulations thereof have sucessfully shown the current dependency of the active particle population [73]. We investigate the more exotic case of polycrystalline particles [74] to check if the concept of transition from particle-by-particle to concurrent intercalation still applies.

We employ the multiphase-field model described in Sec. 2.6, still under the assumptions made for the depth-averaging, to extend the previous simulations. Depth-averaging now implies the rather strong assumptions of perfectly interconnected crystals and equal alignment of the b-axis. As the diffusivities in (100)- and (001)-direction are on the same order of magnitude, we neglect in-plane diffusion anisotropy. Note that the inclusion of orthotropic anisotropy in a single crystal simulation is rather straight forward due to grid-aligned discretization (e.g. using finite difference or finite volume schemes). This is, however, not the case for a polycrystalline section with arbitrary lattice orientations. More elaborate handling of the discretization of diffusion is needed to study the full effect of diffusion anisotropy in future works. A noise term enables the simulation of heterogeneous nucleation without making a priori assumptions about the nucleation site. We follow the procedure sketched in [6] to fit the model parameters which leads to $\varepsilon = 2.5 \, [\text{nm}]$ and $\gamma_{\text{FP-LFP}} = 0.1 \, [J/m^2]$ for the FP-LFP interface. The pre-existing grain boundaries are assumed to have a higher interfacial energy $\gamma_{\text{FP-FP}} = \gamma_{\text{LFP-LFP}} = 3 \cdot \gamma_{\text{FP-LFP}}$ because they are incoherent. Furthermore, we employ the quadratic chemical energy fits displayed in Fig. 1b which are determined by the parameters $A^{\text{FP}} = A^{\text{LFP}} = 150 \cdot RTc_{\max} \, [J/m^3]$, $c_{\min}^{\text{FP}} = 0.06$, $c_{\min}^{\text{LFP}} = 0.94$ and $B^{\text{FP}} = B^{\text{LFP}} = 0$. As the phase transformations are assumed to be limited by ion kinetics (reaction and diffusion instead of attachment kinetics), we set the mobility of the phase-field evolution to $M_{\alpha\beta} = 5 \cdot D^{(100)}$. A polycrystalline section for

the initial simulation setup was prepared by randomized filling employing Voronoi tesselation and subsequent phase evolution under volume conservation [75] such that higher order junctions feature equilibrium angles. We then apply various C-rates to study the influence of particle interaction. First, mechanical influences are neglected and the results for high in-plane diffusion with $\rho = 0.05$ are shown in Fig. 8.
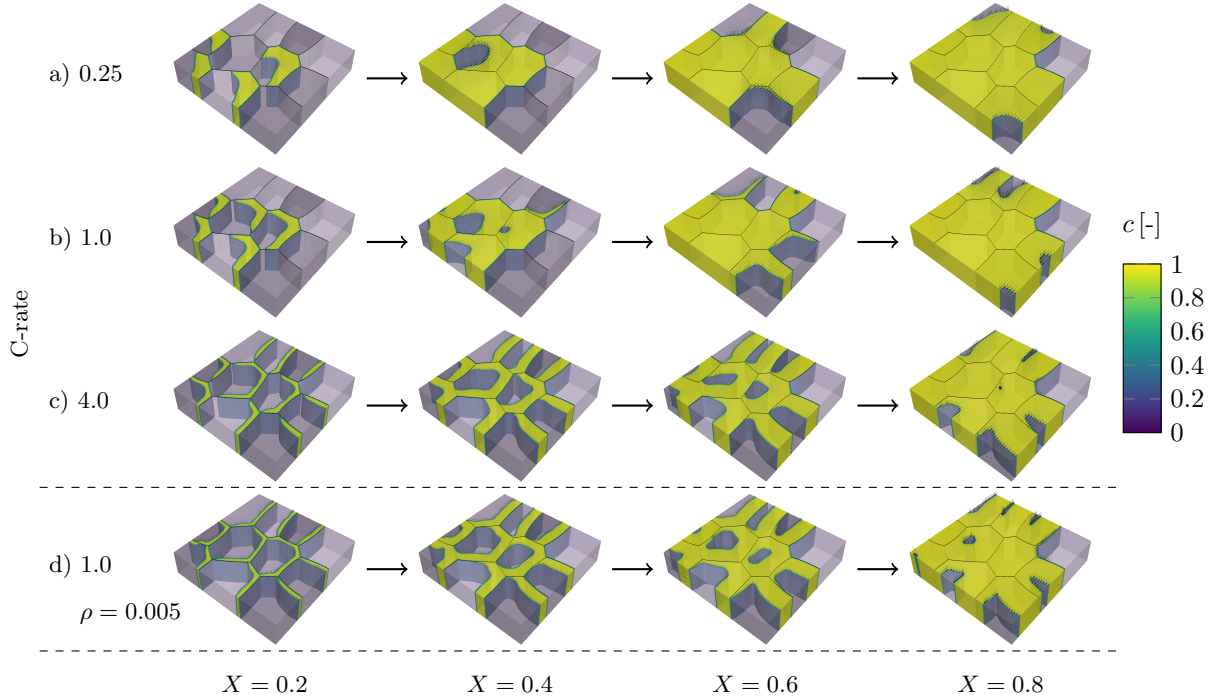

Figure 8: Multi-grain platelet with dimensions $250 \times 250 \times 50\,\mathrm{nm}$ during discharge using the depth-averaged model. X denotes the average filling fraction in $\mathrm{Li}_X\mathrm{FePO}_4$ while the local composition c is indicated by the colorbar. Arrows indicate the magnitude of reaction flux vectors and are scaled to the average reaction flux. The influence of coherency strain is neglected. The top three rows show simulations based on high defect density $\rho = 0.05$ while the bottom row has $\rho = 0.005$.

For all simulations, we observe that nucleation events occuring during cycling mostly happen at higher-order junctions but also at the pre-existing grain boundaries. This is due to the lower nucleation barrier of new phases at the interface [6]. There is a clear trend that higher C-rates lead to more simultaneous nucleation events which is consistent with the observation of higher active particle population in other phase-field studies [69, 73]. At C= 0.25, the filling proceeds in a grain-by-grain manner filling one to four grains at a time. This behaviour reflects the fact that charging particles one-by-one is thermodynamically favourable in the limit of vanishing current [38]. At a C-rate of four, we observe simultaneous nucleation in all but one grain followed by pre-dominantly intra-particle phase separation during the discharging process. In this regime, the diffusivity is high enough for phase separation but not sufficient for relaxation from the intra- to inter-particle phase-separated state. The differences become more evident from the simulation videos in the Supporting Information [42]. Reducing the in-plane diffusivity by one order of magnitude also leads to

more nucleation events. Fig. 8 d) shows the composition evolution with $\rho = 0.005$ at C= 1 for comparison. The resulting pattern formation of high- and low-concentration phases is comparable to the case of higher in-plane diffusion together with higher C-rate in Fig. 8 c).

As we have already observed in the case of the single platelet in Fig. 7, adding the influence of coherency strain stabilizes intermediate composition states to buffer the lattice mismatch between FP and LFP. Nucleation still occurs at multiple junctions and grain boundaries and stress peaks can be observed at the interface of high and low composition regions. In Fig. 9, we investigate the influence of texture, i.e. the distribution of crystallographic orientations , in a multi-grain sample. The considered cases range from complete matching
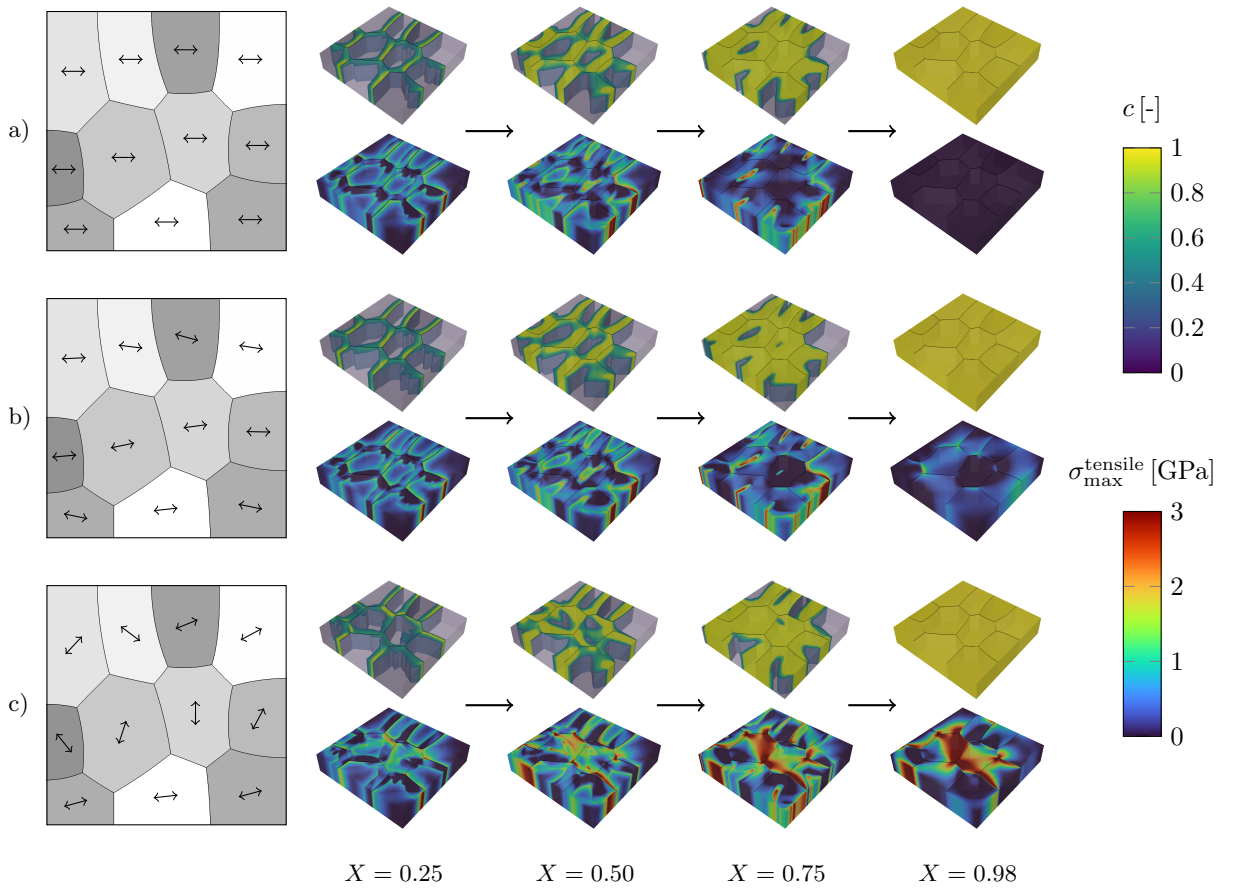

Figure 9: Influence of texture on mechanical stresses during discharge using the depth-averaged model. The multi-grain platelet has dimensions $250 \times 250 \times 50\,\mathrm{nm}$, X denotes the average filling fraction in $\mathrm{Li}_X\mathrm{FePO}_4$ while the local composition c is indicated by the colorbar. Arrows in the multi-grain section on the left indicate the orientation of the a-axis. The c-axis is orthogonal to the arrow while the b-direction of all grains is pointing into the sketched plane.

of crystal alignment (strong texture) in 9 a) to a fully random distribution (no distinct texture) in 9 c). In all cases, we compute the fully three-dimensional stress state resulting from the phase-dependent eigenstrain with traction free surfaces as the mechanical boundary condition.

24

Comparison of the two textured samples (9 a) and b)) shows that the concentration and stress evolution is almost identical upon insertion. This stems from the fact that the phase transformation pathway in this regime is predominantly set by the C-rate and in-plane diffusivity. The biggest difference can be observed in the final state where, in the case of complete orientation alignment, all stresses vanish. For the case of small misalignment between the grains, on the other hand, a residual stress is preserved. Stresses accumulate at grain boundaries where the misorientation of neighbouring grains leads to unequal expansion and contraction within the interfacial region. In the third case of fully random crystal orientations, much higher residual stresses are observed. The two inner grains exhibit especially high tensile stresses due to their misalignment. In the final state, larger domains are subject to tensile stresses above $3\,\mathrm{GPa}$ and stress hotspots can be found at triple junctions with a maximum principle stress of $7.28\,\mathrm{GPa}$. Hotspots of large tensile stresses are already a good indicator for possible fracture of polycrstalline materials. Future simulations could possibly include explicit modelling of fracture mechanics based on a phase-field approach [46, 76, 77].

4. Conclusion

In this work, we discussed a new modeling approach based on the multiphase-field method in the context of previous works and basic modelling assumptions. The multi-grain studies in Sec. 3.4 underline the necessity to account for multiple interacting particles, especially in systems featuring phase transformations. Agglomerates and particle ensembles behave differently compared to isolated single crystals which highlights the importance of electrode morphology design for battery performance. An important step to improve the proposed modeling framework is a thermodynamically sound formulation to account for an electrolyte phase and the electro-chemical reaction in the diffuse interface. The strong ion migration anisotropy of some intercalation compounds needs inclusion of crystal lattice orientation and anisotropic diffusivities to fully capture the occuring transport processes.

We show that the established phase-field models are able to capture spinodal decomposition as a relaxation mechanism and are furthermore able to predict a wide range of strongly coupled effects such as supression of phase separation under sufficient driving force. The newly introduced model extends existing works in the sense that multi-particle interactions including the transition from inter-particle to intra-particle phase separation for increasing C-rates up to complete suppression of phase separation can be modelled. The combination of a thermodynamically consistent model and quantitative material data yields simulation results that are in agreement with experimental observations. LFP has been used as a prominent example in this case but we expect huge potential in the field of post-lithium materials research. Thus, the multi-phasefield approach based on Allen-Cahn equations is reckoned to be promising for the in-depth analysis of phase transformation mechanisms in interacting particle ensembles.

The influence of texture in polycrystalline samples is crucial with regard to mechanical degradation. The

simulations performed in Sec. 3.4 highlight the dependence of stress hotspots on the misorientation of neighboring grains, especially for strongly anisotropic cathode materials like LFP. The question of nano-structure design to reduce residual stresses is even more relevant for layered-oxide materials such as NMC which are typically produced as polycrystals. Studies have shown that open-pored nanostructuring can, among other benefits, increase cycle life as particle fragmentation is reduced [78]. Many promising sodium ion cathode materials are also layered oxides and produced as polycrystals [79]. Due to the larger atomic radius of sodium, many intercalation compounds undergo phase transformations coupled with large volume changes of the crystal lattice upon cycling which increases the probability of mechanical degradation. Morphology optimization by means of computational studies becomes feasible with the proposed framework.

Our main intention is to facilitate the transfer of these methods to other material systems and accelerate materials discovery in the field of electro-chemical energy storage. The close link to atomistic simulations by inclusion of DFT simulation data into our phase-field formulations points to the potential of data transfer across the scales. The reduced one-dimensional models which are used in the P2D modeling approach [62] need to reflect the material anisotropies to fully bridge the gap from the nano- to the cell-scale. The simplified modeling of coherency strains derived in the Supplementary Material [42] and employed in Sec. 3.2, depicts an effective way to include mechanical effects into a reduced Cahn-Hilliard model formulations. This approach in combination with a suitable dimensionality reduction, is considered promising for the inclusion of phase-separating single crystal in P2D methods. Therefore, the developed code is made open for others to be further developed and hopefully improve modeling of battery compounds for accelerated materials discovery.

Appendix A. Thermodynamic pre-factor for Butler-Volmer equation

Modeling of the electro-chemical reaction at the electrode-electrolyte interface is non-trivial, as many of the relevant properties and field variables are difficult to access. There are competing formulations for the thermodynamic pre-factor [39–41], leading to quite different simulation results. We compare $j_0 = k_0 \sqrt{x(1-x)}$ to the approach based on transition state theory for concentrated solutions [24], where

$$j_0 = k_0 \frac{a_+^{1-\alpha} a^\alpha}{\gamma_A}. \tag{A.1}$$

The expression can be simplified, assuming constant activity of Li^+ in the electrolyte ($a_+ = 1$), symmetry of the reaction ($\alpha = 0.5$) and the chemical activity coefficient of the activated state taken to be $\gamma_A = (1-x)^{-1}$. Furthermore inserting the relation $a = \exp(\mu)$ with the definition of diffusion potential in Eq. (14) into Eq. (A.1), the pre-factor reduces to $j_0 = k_0(1-x)\exp(\mu/2)$. The comparison in Fig. A.10 shows how the pre-factor influences the rate-dependent overpotentials.

(a) $j_0 = k_0\sqrt{x(1-x)}$ (b) $j_0 = k_0(1-x)a_+^{1-\alpha}a^\alpha$
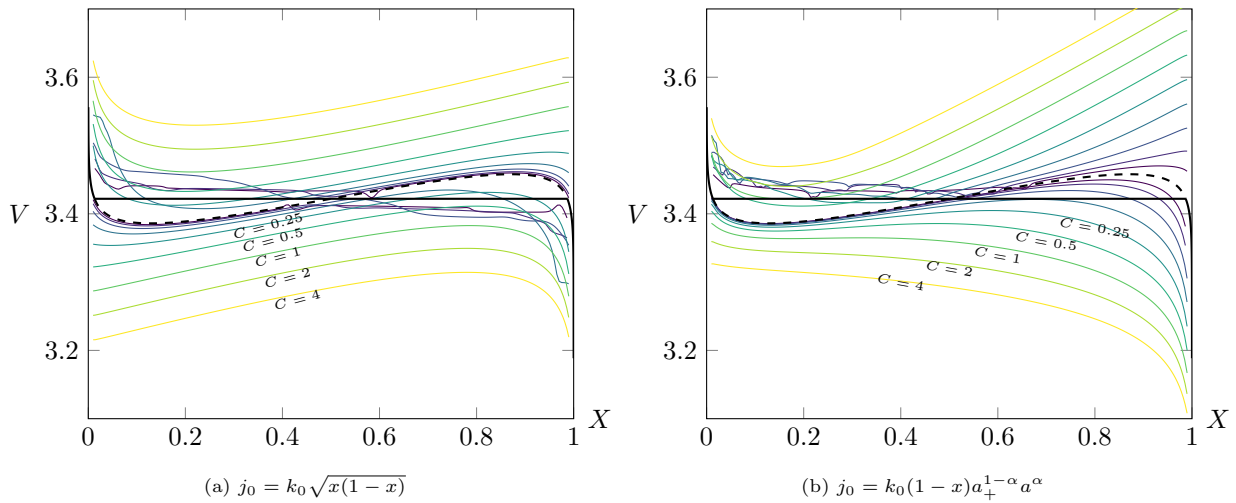
Figure A.10: Comparison of two possible choices to model the thermodynamic pre-factor in the Butler-Volmer equation (classical formulation versus formulation based on Marcus theory). V over X in Li$_X$FePO$_4$ according to Eq. (10) for varying C-rate $C = 2^N$ [1/h] where $N \in [-6, -5, ..., 2]$ and a constant thickness of $H = 50$ nm. The equilibrium case is drawn in black according to Eq. (6). While the classical formulation is completely symmetric in the charge and discharge regime, the formulation based on Marcus theory features auto-catalytic behaviour upon charge and auto-inhibitory behaviour upon discharge [71].

Acknowledgments

References

[1] A.K. Padhi, K.S. Nanjundaswamy, and J.B. Goodenough. Phospho-olivines as Positive Electrode Materials for Rechargeable Lithium Batteries. *Journal of the Electrochemical Society*, 144(4):1188, 1997.

[2] Z. Lu and J.R. Dahn. In Situ X-Ray Diffraction Study of P2-Na2/3Ni1/3Mn2/3O2. *Journal of The Electrochemical Society*, 148(11):A1225, 2001.

[3] P. Moreau, D. Guyomard, J. Gaubicher, and F. Boucher. Structure and Stability of Sodium Intercalated Phases in Olivine FePO 4. *Chemistry of Materials*, 22(14):4126–4128, jul 2010.

[4] R. Malik, A. Abdellahi, and G. Ceder. A Critical Review of the Li Insertion Mechanisms in LiFePO 4 Electrodes. *Journal of The Electrochemical Society*, 160(5):A3179–A3197, 2013.

[5] G.K. Singh, G. Ceder, and M.Z. Bazant. Intercalation dynamics in rechargeable battery materials: General theory and phase-transformation waves in LiFePO4. *Electrochimica Acta*, 53(26):7599–7613, 2008.

[6] S. Daubner, P G Kubendran Amos, E. Schoof, J. Santoki, D. Schneider, and B. Nestler. Multiphase-field modeling of spinodal decomposition during intercalation in an Allen-Cahn framework. *Physical Review Materials*, 5(3):035406, mar 2021.

[7] J. Eiken, B. Böttger, and I. Steinbach. Multiphase-field approach for multicomponent alloys with extrapolation scheme for numerical application. *Physical Review E*, 73(6):066122, jun 2006.

[8] N. Moelans, B. Blanpain, and P. Wollants. An introduction to phase-field modeling of microstructure evolution. *Calphad: Computer Coupling of Phase Diagrams and Thermochemistry*, 32(2):268–294, 2008.

[9] I. Steinbach. Phase-field models in materials science. *Modelling and Simulation in Materials Science and Engineering*, 17(7), 2009.

[10] D.A. Cogswell and M.Z. Bazant. Coherency strain and the kinetics of phase separation in LiFePO 4 nanoparticles. *ACS Nano*, 6(3):2215–2225, 2012.

[11] L. Hong, K. Yang, and M. Tang. A mechanism of defect-enhanced phase transformation kinetics in lithium iron phosphate olivine. *npj Computational Materials*, 5(1):1–9, 2019.

[12] E. Schoof, D. Schneider, N. Streichhan, T. Mittnacht, M. Selzer, and B. Nestler. Multiphase-field modeling of martensitic phase transformation in a dual-phase microstructure. *International Journal of Solids and Structures*, 134:181–194, 2018.

[13] M. Kellner, J. Hötzer, E. Schoof, and B. Nestler. Phase-field study of eutectic colony formation in NiAl-34Cr. *Acta Materialia*, 182:267–277, 2020.

[14] B. Nestler, H. Garcke, and B. Stinner. Multicomponent alloy solidification: phase-field modeling and simulations. *Physical Review E*, 71(4):41609, 2005.

[15] B.C. Han, A. Van Der Ven, D. Morgan, and G. Ceder. Electrochemical modeling of intercalation processes with phase field models. *Electrochimica Acta*, 49(26):4691–4699, 2004.

[16] D. Morgan, A. Van der Ven, and G. Ceder. Li Conductivity in LixMPO4 (M = Mn, Fe, Co, Ni) Olivine Materials. *Electrochemical and Solid-State Letters*, 7(2):A30, 2004.

[17] R. Malik, D. Burch, M.Z. Bazant, and G. Ceder. Particle size dependence of the ionic diffusivity. *Nano Letters*, 10(10):4123–4127, 2010.

[18] T. Maxisch and G. Ceder. Elastic properties of olivine LixFePO4 from first principles. *Physical Review B*, 73(17):174112, may 2006.

[19] A. Abdellahi, O. Akyildiz, R. Malik, K. Thornton, and G. Ceder. Particle-size and morphology dependence of the preferred interface orientation in LiFePO4 nano-particles. *Journal of Materials Chemistry A*, 2(37):15437–15447, 2014.

[20] N.G. Hörmann and A. Groß. Phase field parameters for battery compounds from first-principles calculations. *Physical Review Materials*, 3(5):1–10, 2019.

[21] C. Hin. Kinetic Monte Carlo Simulations of Anisotropic Lithium Intercalation into LixFePO4 Electrode Nanocrystals. *Advanced Functional Materials*, 21(13):2477–2487, jul 2011.

[22] P. Xiao and G. Henkelman. Kinetic Monte Carlo Study of Li Intercalation in LiFePO 4. *ACS Nano*, 12(1):844–851, jan 2018.

[23] E. M. Gavilán-Arriazu, M. P. Mercer, D. E. Barraco, H. E. Hoster, and E. P. M. Leiva. Kinetic Monte Carlo simulations applied to Li-ion and post Li-ion batteries: a key link in the multi-scale chain. *Progress in Energy*, 3(4):042001, oct 2021.

[24] P. Bai, D.A. Cogswell, and M.Z. Bazant. Suppression of phase separation in LiFePO4 nanoparticles during battery discharge. *Nano Letters*, 11(11):4890–4896, 2011.

[25] M. Tang, J.F. Belak, and M.R. Dorr. Anisotropic phase boundary morphology in nanoscale olivine electrode particles. *Journal of Physical Chemistry C*, 115(11):4922–4926, 2011.

[26] M. Huttin. *Phase-field modeling of the infuence of mechanical stresses on charging and discharging processes in lithium ion batteries*. Phd thesis, KIT, 2014.

[27] J.W. Cahn and J.E. Hilliard. Free Energy of a Nonuniform System. I. Interfacial Free Energy. *The Journal of Chemical Physics*, 28(2):258–267, feb 1958.

[28] J.W. Cahn. On spinodal decomposition. *Acta Metallurgica*, 9:795–801, 1961.

[29] M. Plapp. Unified derivation of phase-field models for alloy solidification from a grand-potential functional. *Physical Review E - Statistical, Nonlinear, and Soft Matter Physics*, 84(3):1–15, 2011.

[30] A. Choudhury and B. Nestler. Grand-potential formulation for multicomponent phase transformations combined with thin-interface asymptotics of the double-obstacle potential. *Physical Review E*, 85(2):21602, 2012.

[31] D. Schneider, O. Tschukin, A. Choudhury, M. Selzer, T. Böhlke, and B. Nestler. Phase-field elasticity model based on mechanical jump conditions. *Computational Mechanics*, 55(5):887–901, may 2015.

[32] D. Schneider, E. Schoof, O. Tschukin, A. Reiter, C. Herrmann, F. Schwab, M. Selzer, and B. Nestler. Small strain multiphase-field model accounting for configurational forces and mechanical jump conditions. *Computational Mechanics*, 61(3):277–295, mar 2018.

[33] D. Schneider, E. Schoof, Y. Huang, M. Selzer, and B. Nestler. Phase-field modeling of crack propagation in multiphase systems. *Computer Methods in Applied Mechanics and Engineering*, 312:186–195, dec 2016.

[34] C. Herrmann, D. Schneider, E. Schoof, F. Schwab, and B. Nestler. Phase-Field Model for the Simulation of Brittle-Anisotropic and Ductile Crack Propagation in Composite Materials. *Materials*, 14(17):4956, aug 2021.

[35] M. Späth, C. Herrmann, N. Prajapati, D. Schneider, F. Schwab, M. Selzer, and B. Nestler. Multiphase-field modelling of crack propagation in geological materials and porous media with Drucker-Prager plasticity. *Computational Geosciences*, 25(1):325–343, feb 2021.

[36] S. Chakraborty, P. Kumar, and A. Choudhury. Phase-field modeling of grain-boundary grooving and migration under electric current and thermal gradient. *Acta Materialia*, 153:377–390, 2018.

[37] P.W. Hoffrogge, A. Mukherjee, E.S. Nani, P.G. Kubendran Amos, F. Wang, D. Schneider, and B. Nestler. Multiphase-field model for surface diffusion and attachment kinetics in the grand-potential framework. *Physical Review E*, 103(3):033307, mar 2021.

[38] W. Dreyer, J. Jamnik, C. Guhlke, R. Huth, J. Moškon, and M. Gaberšček. The thermodynamic origin of hysteresis in insertion batteries. *Nature Materials*, 9(5):448–453, 2010.

[39] W. Schmickler and E. Santos. *Interfacial Electrochemistry*. Springer Berlin Heidelberg, Heidelberg, second edition, 2010.

[40] M.Z. Bazant. Theory of chemical kinetics and charge transfer based on nonequilibrium thermodynamics. *Accounts of Chemical Research*, 46(5):1144–1160, 2013.

[41] N. Nadkarni, E. Rejovitsky, D. Fraggedakis, C.V. Di Leo, R.B. Smith, P. Bai, and M.Z. Bazant. Interplay of phase boundary anisotropy and electro-auto-catalytic surface reactions on the lithium intercalation dynamics in LiXFePO4 plateletlike nanoparticles. *Physical Review Materials*, 2(8):1–13, 2018.

[42] See Supplemental Material at [URL will be inserted].

[43] M. Huttin and M. Kamlah. Phase-field modeling of stress generation in electrode particles of lithium ion batteries. *Applied Physics Letters*, 101(13), 2012.

[44] Daniel A. Cogswell and Martin Z. Bazant. Theory of Coherent Nucleation in Phase-Separating Nanoparticles. *Nano Letters*, 13(7):3036–3041, jul 2013.

[45] Michael J. Welland, Dmitry Karpeyev, Devin T. O'Connor, and Olle Heinonen. Miscibility Gap Closure, Interface Morphology, and Phase Microstructure of 3D LixFePO4 Nanoparticles from Surface Wetting and Coherency Strain. *ACS Nano*, 9(10):9757–9771, 2015.

[46] D.T. O'Connor, M.J. Welland, W. Kam Liu, and P.W. Voorhees. Phase transformation and fracture in single LixFePO4 cathode particles: A phase-field approach to Li-ion intercalation and fracture. *Modelling and Simulation in Materials Science and Engineering*, 24(3), 2016.

[47] A.C. Walk, M. Huttin, and M. Kamlah. Comparison of a phase-field model for intercalation induced stresses in electrode particles of lithium ion batteries for small and finite deformation theory. *European Journal of Mechanics, A/Solids*, 48(1):74–82, 2014.

[48] Y. Zhao, B.-X. Xu, P. Stein, and D. Gross. Phase-field study of electrochemical reactions at exterior and interior interfaces in Li-ion battery electrode particles. *Computer Methods in Applied Mechanics and Engineering*, 312:428–446, dec 2016.

[49] I. Steinbach and F. Pezzolla. A generalized field method for multiphase transformations using interface fields. *Physica D: Nonlinear Phenomena*, 134(4):385–393, dec 1999.

[50] AG Khachaturyan. *Theory of Structural Transformations in Solids*. John Wiley & Sons Inc, New York, 1983.

[51] K. Ammar, B. Appolaire, G. Cailletaud, and S. Forest. Combining phase field approach and homogenization methods for modelling phase transformation in elastoplastic media. *European Journal of Computational Mechanics*, 18(5-6):485–523, jan 2009.

[52] P.-C. A. Simon, L. K. Aagesen, A. T. Motta, and M. R. Tonks. The effects of introducing elasticity using different interpolation schemes to the grand potential phase field model. *Computational Materials Science*, 183(April):109790, oct 2020.

[53] T. Zhang and M. Kamlah. Microstructure evolution and intermediate phase-induced varying solubility limits and stress reduction behavior in sodium ion batteries particles of NaXFePO4 (0¡x¡1). *Journal of Power Sources*, 483(October 2020):229187, jan 2021.

[54] L.K. Aagesen, Y. Gao, D. Schwen, and K. Ahmed. Grand-potential-based phase-field model for multiple phases, grains, and chemical components. *Physical Review E*, 98(2):1–16, 2018.

[55] J. Eiken. *A Phase-Field Model for Technical Alloy Solidification*. phdthesis, RWTH Aachen, 2009.

[56] G. Chen, X. Song, and T.J. Richardson. Electron microscopy study of the LiFePO 4 to FePO 4 phase transition. *Electrochemical and Solid-State Letters*, 9(6):295–298, 2006.

[57] M. Fleck, H. Federmann, and E. Pogorelov. Phase-field modeling of Li-insertion kinetics in single LiFePO4-nano-particles for rechargeable Li-ion battery application. *Computational Materials Science*, 153:288–296, 2018.

[58] L. Wang, F. Zhou, Y. S. Meng, and G. Ceder. First-principles study of surface properties of LiFeP O4: Surface energy, structure, Wulff shape, and surface redox potential. *Physical Review B - Condensed Matter and Materials Physics*, 76(16):1–11, 2007.

[59] C.A.J. Fisher and M.S. Islam. Surface structures and crystal morphologies of LiFePO4: Relevance to electrochemical behaviour. *Journal of Materials Chemistry*, 18(11):1209–1215, 2008.

[60] S. Yang, P. Y. Zavalij, and S.M. Whittingham. Hydrothermal synthesis of lithium iron phosphate cathodes. *Electrochemistry Communications*, 3(9):505–508, sep 2001.

[61] G. Chen, X. Song, and T.J. Richardson. Metastable solid-solution phases in the lifepo4/fepo4 system. *Journal of The Electrochemical Society*, 154(7):A627, 2007.

[62] R.B. Smith and M.Z. Bazant. Multiphase Porous Electrode Theory. *Journal of The Electrochemical Society*, 164(11):E3291–E3310, jun 2017.

[63] R. Malik, F. Zhou, and G. Ceder. Kinetics of non-equilibrium lithium incorporation in LiFePO4. *Nature Materials*, 10(8):587–590, 2011.

[64] J.W. Cahn. Phase Separation by Spinodal Decomposition in Isotropic Systems. *The Journal of Chemical Physics*, 42(1):93–99, jan 1965.

[65] A. Abdellahi, O. Akyildiz, R. Malik, K. Thornton, and G. Ceder. The thermodynamic stability of intermediate solid solutions in LiFePO 4 nanoparticles. *Journal of Materials Chemistry A*, 4(15):5436–5447, 2016.

[66] L. Hong, L. Li, Y.K. Chen-Wiegart, J. Wang, K. Xiang, L. Gan, W. Li, F. Meng, F. Wang, J. Wang, Y.M. Chiang, S. Jin, and M. Tang. Two-dimensional lithium diffusion behavior and probable hybrid phase transformation kinetics in olivine

lithium iron phosphate. *Nature Communications*, 8(1), 2017.

[67] Y. Zhang and M. Tang. Stress-Induced Intercalation Instability. *Acta Materialia*, 201:158–166, dec 2020.

[68] C. Delmas, M. Maccario, L. Croguennec, F. Le Cras, and F. Weill. Lithium deintercalation in LiFePO4 nanoparticles via a domino-cascade model. *Nature Materials*, 7(8):665–671, 2008.

[69] Y. Li, H. Chen, K. Lim, H. D. Deng, J. Lim, D. Fraggedakis, P. M. Attia, S. C. Lee, N. Jin, J. Moškon, Z. Guan, W. E. Gent, J. Hong, Y.-S. Yu, M. Gaberšček, M. S. Islam, M. Z. Bazant, and W. C. Chueh. Fluid-enhanced surface diffusion controls intraparticle phase transformations. *Nature Materials*, 17(10):915–922, oct 2018.

[70] D. Fraggedakis, N. Nadkarni, T. Gao, T. Zhou, Y. Zhang, Y. Han, R.M. Stephens, Y. Shao-Horn, and M.Z. Bazant. A scaling law to determine phase morphologies during ion intercalation. *Energy & Environmental Science*, 13(7):2142–2152, 2020.

[71] M.Z. Bazant. Thermodynamic stability of driven open systems and control of phase separation by electro-autocatalysis. *Faraday Discussions*, 199:423–463, 2017.

[72] William C. Chueh, Farid El Gabaly, Joshua D. Sugar, Norman C. Bartelt, Anthony H. McDaniel, Kyle R. Fenton, Kevin R. Zavadil, Tolek Tyliszczak, Wei Lai, and Kevin F. McCarty. Intercalation Pathway in Many-Particle LiFePO 4 Electrode Revealed by Nanoscale State-of-Charge Mapping. *Nano Letters*, 13(3):866–872, mar 2013.

[73] Y. Li, F. El Gabaly, T. R. Ferguson, R. B. Smith, N. C. Bartelt, J. D. Sugar, K. R. Fenton, D. A. Cogswell, A. L. D. Kilcoyne, T. Tyliszczak, M. Z. Bazant, and W. C. Chueh. Current-induced transition from particle-by-particle to concurrent intercalation in phase-separating battery electrodes. *Nature Materials*, 13(12):1149–1156, dec 2014.

[74] J. Zhu, J. Fiore, D. Li, N. M. Kinsinger, Q. Wang, E. DiMasi, J. Guo, and D. Kisailus. Solvothermal Synthesis, Development, and Performance of LiFePO 4 Nanostructures. *Crystal Growth & Design*, 13(11):4659–4666, nov 2013.

[75] B. Nestler, F. Wendler, M. Selzer, B. Stinner, and H. Garcke. Phase-field model for multiphase systems with preserved volume fractions. *Physical Review E*, 78(1):011604, jul 2008.

[76] M. Klinsmann, D. Rosato, M. Kamlah, and R.M. McMeeking. Modeling crack growth during Li insertion in storage particles using a fracture phase field approach. *Journal of the Mechanics and Physics of Solids*, 92:313–344, 2016.

[77] Yang Bai, David A. Santos, Shahed Rezaei, Peter Stein, Sarbajit Banerjee, and Bai-Xiang Xu. A chemo-mechanical damage model at large deformation: numerical and experimental studies on polycrystalline energy materials. *International Journal of Solids and Structures*, 228:111099, 2021.

[78] Marcus Müller, Luca Schneider, Nicole Bohn, Joachim R. Binder, and Werner Bauer. Effect of Nanostructured and Open-Porous Particle Morphology on Electrode Processing and Electrochemical Performance of Li-Ion Batteries. *ACS Applied Energy Materials*, 4(2):1993–2003, feb 2021.

[79] Hai Hu, Ke Tang, Shuang Cao, Xiukang Yang, and Xianyou Wang. Synthesis and electrochemical properties of P2–Na2/3[Ni1/3Mn2/3]O2 microspheres as cathode materials for sodium-ion batteries. *Journal of Alloys and Compounds*, 859(xxxx):157768, apr 2021.